

## AE9, AP9 and SPM: New Models for Specifying the Trapped Energetic Particle and Space Plasma Environment

G.P. Ginet · T.P. O'Brien · S.L. Huston · W.R. Johnston · T.B. Guild · R. Friedel · C.D. Lindstrom · C.J. Roth · P. Whelan · R.A. Quinn · D. Madden · S. Morley · Yi-Jiun Su

Received: 10 September 2012 / Accepted: 10 January 2013  
© US Government 2013

**Abstract** The radiation belts and plasma in the Earth's magnetosphere pose hazards to satellite systems which restrict design and orbit options with a resultant impact on mission performance and cost. For decades the standard space environment specification used for spacecraft design has been provided by the NASA AE8 and AP8 trapped radiation belt models. There are well-known limitations on their performance, however, and the need for a new trapped radiation and plasma model has been recognized by the engineering community for some time. To address this challenge a new set of models, denoted AE9/AP9/SPM, for energetic electrons, energetic protons and space plasma has been developed. The new models offer significant improvements including more detailed spatial resolution and the quantification of uncertainty due to both space weather and instrument errors. Fundamental

---

G.P. Ginet (✉)  
MIT Lincoln Laboratory, 244 Wood Street, Lexington, MA 20420, USA  
e-mail: [gregory.ginet@ll.mit.edu](mailto:gregory.ginet@ll.mit.edu)

T.P. O'Brien · T.B. Guild  
The Aerospace Corporation, 15409 Conference Center Drive, Chantilly, VA 20151, USA

S.L. Huston · D. Madden  
The Institute for Scientific Research, 400 St. Clement's Hall, Boston College, 140 Commonwealth Avenue, Chestnut Hill, MA 02467, USA

*Present address:*  
S.L. Huston  
Atmospheric and Environmental Research, Incorporated, 131 Hartwell Avenue, Lexington, MA 02421, USA

W.R. Johnston · C.D. Lindstrom · Y.-J. Su  
Space Vehicles Directorate, Air Force Research Laboratory, Kirtland AFB, NM 87117, USA

C.J. Roth · P. Whelan · R.A. Quinn  
Atmospheric and Environmental Research, Incorporated, 131 Hartwell Avenue, Lexington, MA 02421, USA

R. Friedel · S. Morley  
Los Alamos National Laboratory, PO Box 1663, Los Alamos, NM 87545, USA

to the model design, construction and operation are a number of new data sets and a novel statistical approach which captures first order temporal and spatial correlations allowing for the Monte-Carlo estimation of flux thresholds for user-specified percentile levels (e.g., 50th and 95th) over the course of the mission. An overview of the model architecture, data reduction methods, statistics algorithms, user application and initial validation is presented in this paper.

**Keywords** Radiation belt modeling · Energetic trapped particles · Space environment climatology · Space weather

## 1 Introduction

Since the launch of simple Geiger counters into space on the first Explorer satellites in 1958 and the subsequent discovery of the Van Allen radiation belts, there have been ongoing efforts to model the space radiation environment. These efforts were—and still are—driven not only by scientific curiosity, but also by the practical need of engineers to understand better and mitigate the significant radiation hazards to spacecraft reliability and survivability. Many anomaly resolution reports and several scientific studies have shown that there is a direct association between the dynamic radiation environment and system or sub-system performance (e.g. Wrenn and Sims 1996; Koons et al. 2000; Brautigam 2002). Spacecraft systems and discrete component performance may gradually deteriorate with accumulated dose or may experience abrupt failure (temporary or permanent) due to discrete events associated with Single Event Effects (SEEs) or electrostatic discharge. The radiation environment specification to which system engineers design is a critical factor driving capability versus survivability tradeoffs. Spacecraft flown in orbits where a more severe radiation environment is anticipated require more expensive radiation hardened components and/or greater shielding mass which constrain launch options, limit performance and drive costs higher.

The first definitive empirical models of the radiation belts were sponsored by the National Aeronautics and Space Administration (NASA) and developed in the 1960s–1970s to represent the average radiation environment during the minimum and maximum phase of the solar cycle. They have been incrementally updated since then, the most recent proton and electron models being AP8 and AE8, respectively (Sawyer and Vette 1976; Vette 1991a, 1991b; Fung 1996). These radiation belt models are still widely used, having enjoyed close to three decades as industry's de facto standard. However, there are well-known limitations on their validity including the under-prediction of dose for orbits in the “slot region”, i.e. low inclination orbits between about 6000–12000 km, and no coverage of the hot and cold plasma populations below 0.1 MeV (Fung 1996; Gussenhoven et al. 1994; Daly et al. 1996; Armstrong and Colborn 2000; Fennell et al. 2003; Brautigam et al. 2004). The former limitation is especially relevant to dose arising from long-lived higher energy protons ( $>40$  MeV) and electrons ( $>1$  MeV) injected during geomagnetic storms. In addition, the models are simple averages representing either solar maximum (AP8/AE8 MAX) or minimum (AP8/AE8 MIN) with no error bars or cumulative probability distributions provided. A broad consensus has been building over the past decades among both engineers and scientists that a more accurate, comprehensive, and up-to-date space radiation environment model is needed. Modern design and systems engineering techniques require models with error bars, finite-time duration probability distributions, and a larger spectral range, especially as increasingly complex technologies are flown and missions are being considered for non-traditional orbit regimes.

The development of a global space radiation model such as the AP8 or AE8 is a tremendous effort involving the analysis and combination of data sets from numerous missions over periods of time measured in solar cycles. Progress has been made on some fronts by developing models using data acquired onboard the CRRES (Meffert and Gussenhoven 1994; Brautigam and Bell 1995), NOAA/TIROS (Huston et al. 1996; Huston 2002), LANL-GEO (Boscher et al. 2003; Sicard-Piet et al. 2008), SAMPEX (Heynderickx et al. 1999) and Polar (Roeder et al. 2005) satellites. Data assimilative techniques that ingest a variety of data sets to drive physics-based models have also been developed (Bourdarie et al. 2009; Reeves et al. 2012). Whereas the NASA models span the entire inner magnetosphere over a very wide range of energies, these more recent models face various limitations, either in energy range, spatial range (e.g., exclusively at geosynchronous orbit (GEO), medium-Earth orbit (MEO) or low-Earth orbit (LEO)), temporal range (limited to a small portion of the solar cycle), or possibly all three. Although newer individual models may be an improvement for the restricted parameter range to which they apply, it is likely that the NASA models will remain the industry standard until the space physics community develops a single, comprehensive and engineer-friendly replacement model with increased functionality addressing the known deficiencies.

To meet this need the National Reconnaissance Office (NRO) and the Air Force Research Laboratory (AFRL) have supported an effort to develop a new set of models. Denoted “AE9” for trapped energetic electrons, “AP9” for trapped energetic protons and “SPM” for space plasma, the naming continues the “AE”, “AP” convention to maintain an association of functional purpose, i.e. use in space system design. The project has been led by principal investigators from the Aerospace Corporation and MIT Lincoln Laboratory and has involved personnel from AFRL, Boston College, Atmospheric and Environmental Research (AER) and Los Alamos National Laboratory. Development of Version 1.0 (V1.0) of AE9/AP9/SPM was under the auspices of the NRO Proton Spectrometer Belt Research (PSBR) program which also supported the development of the Relativistic Proton Spectrometer (RPS) instruments (Mazur et al. 2012) currently flying on the Van Allen Probes (formerly Radiation Belt Storm Probes, or RBSP). Future versions of the model are expected to include data from RPS as well as the many other particle and plasma detectors on the Van Allen Probes. Furthermore, with AE9/AP9/SPM source code and data sets released in the public domain it is hoped that the national and international radiation belt communities will participate in expanding the data sets and analysis, perhaps working together through an organization such as the National Geophysical Data Center or the Committee on Space Research (COSPAR) Panel on Radiation Belt Models (PRBEM), so as to truly maintain a continually improving standard radiation belt model (perhaps with a new name).

The purpose of this document is to present an overview of AE9/AP9/SPM V1.0 (publicly released in September 2012) for a general audience including both engineers interested in understanding what is behind the application and space scientists interested in contributing data sets and algorithms for future versions. Over five years in development (O’Brien 2005; Ginet et al. 2008; Huston et al. 2009) the model comprises 33 satellite data sets, is comprehensively cross-calibrated, makes extensive use of spectral inversion techniques and introduces a new statistical methodology for combining the data to produce realistic probabilities of occurrence for varying flux levels along a user-defined orbit. Section 2 reviews the requirements for the model as gleaned from the satellite design community. Coordinate systems and associated grids used in the model are discussed in Sect. 3. Data set processing techniques and cross-calibration are outlined in Sect. 4. The architecture and construction of the model is described in Sect. 5 to include discussion of flux maps, the time-evolution algorithm and user-application. A comparison of V1.0 output to other models and data sets

**Table 1** Prioritized list of space particle specification requirements for AE9/AP9/SPM. Parentheses indicate higher priority subsets

Priority	Species	Energy	Location	Period	Effects
1	Protons	>10 MeV (>80 MeV)	LEO & MEO	Mission	Dose, SEE, DD, nuclear activation
2	Electrons	>1 MeV	LEO, MEO & GEO	5 min, 1 hr, 1 day, 1 week & mission	Dose, internal charging
3	Plasma	30 eV–100 keV	LEO, MEO & GEO	5 min, 1 hr, 1 day, 1 week & mission	Surface charging, dose
4	Electrons	100 keV–1 MeV	MEO & GEO	5 min, 1 hr, 1 day, 1 week & mission	Internal charging, dose
5	Protons	1 MeV–10 MeV (5–10 MeV)	LEO, MEO & GEO	Mission	Dose

is presented in Sect. 6 and the paper concludes with a summary in Sect. 7. A comprehensive discussion of all the components can be found in the V1.0 Requirements Specification (Ginet and O'Brien 2010), Technical Documentation (Johnston et al. 2013) and User's Guide (Roth et al. 2013).

## 2 Requirements

To determine the specific requirements for AE9/AP9/SPM, input was avidly solicited from the spacecraft engineering community. Several workshops and meetings on the topic were held to include a series of Space Environment Effect Working Groups (SEEWG) sponsored by the Space Technology Alliance, the NASA Living with a Star Working Group Meeting on New Standard Radiation Belt and Space Plasma Models for Spacecraft Engineering (Lauenstein et al. 2005) and a special session at the 2007 NOAA Space Weather Workshop (Radiation Models 2007). In addition, feedback has been received via email and through the Radiation Specifications Forum Website (Radiation Specifications 2007) hosted by NASA to support the effort. Results from the outreach efforts have been integrated, refined and prioritized by the AE9/AP9/SPM team. Table 1 summarizes the findings in terms of priority, species, energy, location and time resolution. Energy ranges in parentheses indicate areas with especially poor coverage in current models. More details can be found in Ginet and O'Brien (2010).

There has been a universal emphasis from the workshops on the need for an authoritative new model recognized by spacecraft buyers and relatively easy-to-use by spacecraft engineers. Given their role in limiting total system lifetimes, energetic ions (10–500 MeV) and electrons (>1 MeV) in the inner magnetosphere ( $\sim$ 400–15000 km altitude) were the primary concern. Models of the poorly characterized lower energy plasma environment (<10 keV) were also a high priority considering the large surface areas and novel materials and coatings under consideration for use in modern space systems. Better characterization of the dynamic MeV electrons (>0.5 MeV) in the slot and outer zone (6000–36000 km altitude) was also universally recognized as important for improving designs to withstand deep dielectric charging events. Relatively low energy protons (1–10 MeV) can cause dose degradation of solar panels and are not yet adequately specified.

In addition to the extended spectral ranges, the new model must also improve upon the statistical description of the space particle distributions. Some regions of energy-location-geophysical activity phase space will be much more accurately described than others and error bars and confidence levels are needed to reflect the uncertainties. Cumulative probability distributions of the flux values time-averaged over different periods (e.g. the 95th percentile of the >1.0 MeV, 12 hour averaged electron flux) are a necessity. The periods of interest are listed in column 5 of Table 1. This is a challenging task considering that the specification must be produced for an arbitrary orbit within the magnetosphere from a model constructed with data from a relatively small number of satellites. Indeed, for V1.0 the resolution for modeling temporal variations at a fixed location is limited to 1 day for electrons, 1 week for protons and is not explicitly captured (other than in the spread of the distribution function) for the plasma. Techniques such as the “sample solar cycle” (see Sect. 7) need to be considered for future versions of the model. For most orbits, variation on finer time scales is dominated by vehicle motion, which is accounted for in the model application at run time.

### 3 Reference Grids

The empirical basis of the AE9/AP9/SPM models is a set of flux maps derived from data measured by particle detectors and dosimeters onboard satellites traversing the radiation belts. Flux map construction requires that many individual flux measurements taken over a large extent of space and a long time span be mapped to a reference grid defined in the context of a specific coordinate system or systems. A judicious choice of coordinate system facilitates the systematic comparison and combination of the data and can significantly reduce spread of flux distribution functions within each grid bin. In particular, coordinates that are invariant over the drift-bounce motion of a particle allow a local angle-resolved flux measurement to be mapped to a 3-D surface, and measurements along an elliptical satellite orbit can therefore cover a 3-D volume.

A wide variety of coordinate systems are available, each with advantages and disadvantages (cf. Cabrera and Lemaire 2007). For AE9/AP9/SPM the primary coordinates are:

- (a) the particle energy  $E$ ,
- (b) the modified second adiabatic invariant  $K$  capturing the particle’s bounce motion,

$$K = \int_{s_m}^{s_{m'}} [B_m - B(s)] ds, \quad (1)$$

where  $B$  is the magnitude of the magnetic field along the particle trajectory  $s$  following a magnetic field line and  $B_m$  is the magnetic field at the particle mirror points  $s_m, s_{m'}$ ,

- (c) the third adiabatic invariant  $\Phi$  capturing the particle’s drift motion,

$$\Phi = \oint_C d\mathbf{L} \cdot \mathbf{A} = \oint_S d\mathbf{a} \cdot \mathbf{B} \quad (2)$$

where  $\mathbf{A}$  is the magnetic vector potential,  $C$  is a curve encompassing the entire drift shell of the particle,  $\mathbf{B}$  is the magnetic field and  $S$  is the area outside the drift shell (Roederer 1970; Schulz 1996).

To more accurately map variations in particle distributions across the Earth’s magnetic epochs the  $(K, \Phi)$  coordinates were chosen. However, the energy  $E$  was chosen instead of the first adiabatic invariant  $\mu$  ( $\mu = p_\perp^2/(2mB)$ , where  $p_\perp$  is the particle perpendicular momentum and  $m$  the mass) since most detector channels measure a range of both energy

and pitch-angle  $\alpha$ , making the spread of measured  $\mu$  much wider than just the spread in  $E$ . The more intuitive Roederer  $L$ -shell  $L^*$  is calculated from  $\Phi$  at a given magnetic epoch according to,

$$L^* = \frac{2\pi k_0}{\Phi}, \quad (3)$$

where  $k_0$  is the magnetic dipole parameter equal to  $\mu_0 M_E / (4\pi)$  with  $\mu_0$  the magnetic permeability of free space and  $M_E$  the Earth's dipole moment.

For all coordinate and mapping calculations, the Olson-Pfizer Quiet model (OPQ77) (Olson and Pfizer 1977) was used for the external magnetic field and the International Geophysical Reference Field (IGRF) model (IGRF 2012) was used for the internal magnetic field. The IGRF was evaluated at the epoch appropriate for when the data was taken (for model construction) or for the orbit of interest (for user application). The OPQ77 model represents all major magnetospheric current systems and is valid for all tilt angles, i.e., angles of incidence of the solar wind on the dipole axis, and accurately represents the total magnetospheric magnetic field for conditions of low magnetic activity and to a geocentric distance of  $15 R_E$  or to the magnetopause. OPQ77 has been shown to be a good average model for the inner magnetosphere (Jordan 1994; McCollough et al. 2008). Although the data used in AE9/AP9/SPM were taken at all levels of magnetospheric activity, it was decided that using an activity-dependent model would be inappropriate. If an activity-dependent field model were used to map the data, the same field model would be required to “un-map” the data for a specific application. Since a user would not know *a-priori* what the activity level would be for a future mission, using such a field model would not have any practical benefit. Therefore, any deviations associated with calculating the mapping coordinates with the OPQ77 model compared to a “truer” magnetic field model are manifested in the spread in the particle distribution within each grid bin and captured by the distribution function parameterization of the flux maps (Sect. 5.1).

There are many advantages to using the adiabatic invariants as coordinates but there are also several disadvantages. For example, at low altitudes the particle flux is controlled more by the thermospheric neutral density than by the magnetic field; thus the flux is a strong function of altitude and is also affected by the density variation over the solar cycle. Another complication is the difference between the drift loss cone and the bounce loss cone. Electrons in particular can be scattered onto drift shells which intersect the surface of the Earth at some point. As the electrons drift eastward eventually they are lost due to atmospheric interactions when the local bounce loss cone becomes equal to the drift loss cone. Although these electrons are not permanently trapped, they are a persistent population and should be included in the trapped particle models. For these reasons the  $(E, K, \Phi)$  coordinate system does a poor job representing flux variations in and near the loss-cone. To overcome this limitation an additional coordinate  $h_{min}$ , defined as the minimum altitude a particle reaches during its drift-bounce orbit, has been introduced in AE9/AP9/SPM to map the region below 1000 km. Obtained as a by-product of the  $\Phi$  computation,  $h_{min}$  is much better than  $\Phi$  for tracking variations in the particle distributions at low altitudes where the flux gradients are large.

Adiabatic coordinates are also less useful for the lower energy plasma where there is a strong magnetic local time (MLT) dependence and effects from electric fields and plasma waves. Consequently, the more traditional McIlwain  $L$ -shell  $L_m$  (McIlwain 1961) and equatorial pitch angle  $\alpha_{eq}$  will be used for the space plasma models instead of  $(K, \Phi)$ . Though MLT variations are substantial for energies less than approximately 100 keV, the main purpose of the SPM is to establish the statistics of particle flux exposure for satellites on mission

time scales, i.e. usually much longer than one day. To avoid the overhead of tracking another degree of freedom in V1.0, the MLT variations of the plasma have not been included in the SPM and are left to future versions. Because the data and simulation capabilities are not yet available to represent the spatiotemporal covariances of plasmas, the statistical linear regression model (Sect. 5.2) has also not been developed for plasmas in V1.0.

Table 2 summarizes parameters for the  $(E, K, \Phi)$ ,  $(E, K, h_{min})$  and  $(E, L_m, \alpha_{eq})$  reference grids used in V1.0. The bin size (i.e. distance between grid points) was chosen to be small enough to provide adequate spatial and spectral resolution, yet large enough to contain a statistically significant number of measurements. Grid spacing for  $(K, \Phi)$  was selected to be uniform in  $K^{1/2}$  and  $\log_{10}(\Phi)$  to improve resolution near the magnetic equator (small values of  $K$ ) and at large values of  $\Phi$  (the inner zone). Note that  $h_{min}$  includes negative values to accommodate particles not in the bounce loss cone for some range of longitudes, but definitely in the drift loss cone. Energy resolution is a mix of both linear and logarithmic with the specific grid values chosen to be consistent with the AP8, AE8, and CAMMICE/MICS models. Component models of SPM are denoted SPMH, SPMHE, SPMO and SPME representing the hydrogen, helium, oxygen and electron constituents, respectively. For SPME the grid is consistent with the LANL/MPA data set (Sect. 4).

As an illustration of the reference grid coverage Fig. 1 shows the median 0.5 MeV electron flux from the AE9 model mapped in the  $(E, K, \Phi)$  and  $(E, K, h_{min})$  grids. In Fig. 1a the y-axis ( $K = 0$ ) is the magnetic equator, and the loss cone is the boundary with the white region, where fluxes are zero. The inner and outer zones are clearly visible as regions of high flux centered at  $\log_{10} \Phi$  values of about 0.05 and -0.4, respectively, with the slot region in between. The grey lines indicate the approximate location of the  $h_{min} = 0$  (upper) and  $h_{min} = 1000$  km (lower) contour, the latter being the upper boundary of Fig. 1b. Also shown in the figures are contours of the traditional  $(L_m, B/B_0)$  coordinates (used in the AP8/AE8 and CRRES models, for example), where  $B$  is the magnitude of the magnetic field at a point along the field line corresponding to  $L_m$  and  $B_0$  is the magnitude of the field at the magnetic equator along the same field line. It can be seen from Fig. 1b that using  $h_{min}$  as a coordinate gives much better resolution of the fluxes at low altitudes (or near the loss cone) where the neutral density and consequently altitude becomes a dominant ordering parameter.

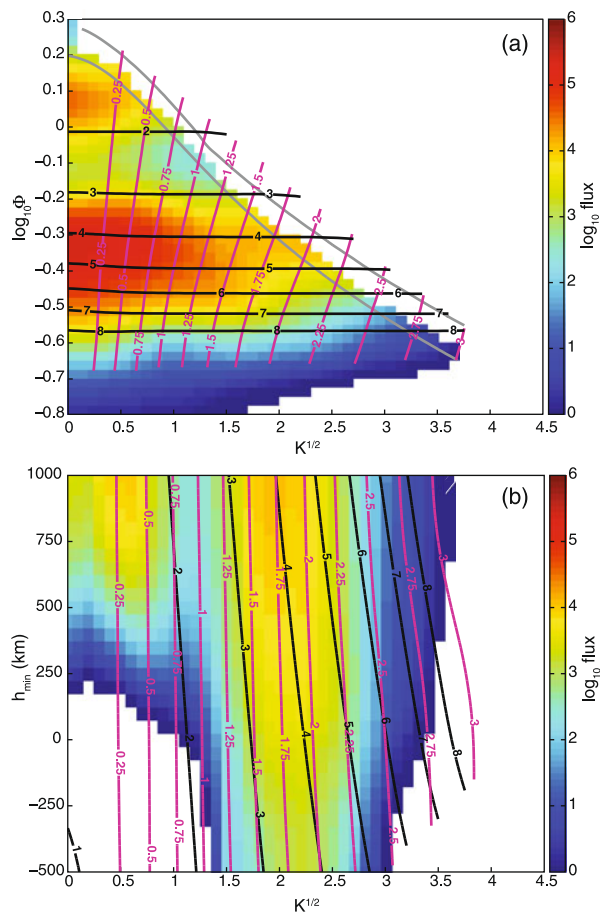
To compute the reference coordinates along the ephemerides of the satellites supplying data to the model the IRBEM-LIB (IRBEM 2012) library of functions was used. Ephemeris data (latitude, longitude, altitude, universal time) were input and the  $K, \Phi, h_{min}, L_m$  and  $\alpha_{eq}$  parameters were output. A modification of IRBEM-LIB was required to calculate  $h_{min}$  in addition to  $\Phi$  and to perform the calculation even if the drift shell dipped below the surface of the Earth. The parameters were calculated for discrete local pitch angles at 10 degree increments between 0 and 90 degrees. If higher resolution was required (e.g. for high pitch-angle resolution sensors) the above computed values were interpolated.

Calculation of the drift shells needed to evaluate  $\Phi$  and  $h_{min}$  is a computer time-consuming process. Direct computation with the IRBEM-LIB routines was sufficient for construction of the flux maps since there are a relatively small number of ephemerides to compute (Sect. 4). However, in the general application where a user might evaluate many orbits for long periods of time the computational load to convert the flux map coordinates can quickly become unrealistic. A neural network interpolation algorithm was therefore developed to produce  $\Phi$  and  $h_{min}$  without the computational expense of integrating over an entire drift shell. For a given satellite position and detector look direction the inputs include the Universal Time (UT), day of year, modified Julian day,  $I (= K/\sqrt{B})$  and  $B_m$  thus requiring a trace of the field line only. A similar approach was used by Koller et al. (2009) and Koller and Zaharia (2011) for active magnetic field models. The neural network is an integral part

**Table 2** Summary of the coordinate grids used in AE9/AP9/SPM. Square brackets denotes the units of the quantity inside

Model	Species	Energy	High Altitude Grid		Low Altitude Grid	
			2nd Inv.	3rd Inv.	2nd Inv.	3rd Inv.
AE9	e <sup>-</sup>	0.04–10 MeV 21 channels	$0 \leq K^{1/2} \leq 4.5$ $\Delta(K^{1/2}) = 0.1$ [K] = $G^{1/2} R_E^2$	$0.8 \leq \log_{10} \Phi \leq 0.3$ $\Delta(\log_{10} \Phi) = 0.025$ [\Phi] = $G^{1/2} R_E^2$	$0 \leq K^{1/2} \leq 4.5$ $\Delta(K^{1/2}) = 0.1$ [K] = $G^{1/2} R_E$	$-500 < h_{min} < 1000$ km $\Delta h_{min} = 50$ km
AP9	H <sup>+</sup>	0.1–400 MeV 22 channels				$0 < h_{min} < 1000$ km $\Delta h_{min} = 50$ km
SPME	e <sup>-</sup>	1–40 keV 16 channels	$5 \leq \alpha_{eq} \leq 85^\circ$ $\Delta\alpha_{eq} = 10^\circ$	$2 \leq L_m \leq 10$ $\Delta L_m = 0.5$	N/A	
SPMH	H <sup>+</sup>	1.15–164 keV 12 channels				
SPMHE	He <sup>+</sup>					
SPMO	O <sup>+</sup>					

**Fig. 1** The (a) ( $K, \Phi$ ) and (b) ( $K, h_{min}$ ) grids used in AE9/AP9 with the median fluxes of 0.5 MeV electrons from AE9 shown. For reference the black and purple lines represent contours of constant ( $L_m, B/B_0$ ), i.e. the coordinates used in many historical models. Grey lines in (a) are contours of  $h_{min} = 0$  and  $h_{min} = 1000$  km in ( $K, \Phi$ ) space



of the AE9/AP9 software allowing  $\Phi$  and  $h_{min}$  to be calculated almost as quickly as  $L_m$ . The algorithm is augmented with boundary models that specify the location of the loss cone at low altitudes and the onset of anomalous high altitude orbits not modeled, i.e. Shabansky orbits appearing on field lines with multiple magnetic minima (Shabansky 1971) and drift orbits intersecting the magnetopause.

#### 4 Data

The AP9/AE9/SPM models are derived from measurements made over an extended period of time by particle detectors and dosimeters on board many satellites in a variety of orbits. Table 3 lists the satellites utilized and for each gives the particular sensor, orbital regimes spanned by the measurements, detector energy ranges and periods of coverage. Acronyms are defined in Appendix A. The raw data for each satellite typically comes as a set of counts per second recorded over a relatively small measurement interval (seconds to several minutes) for several differential or integral energy channels and perhaps several narrow or wide

**Table 3** Satellites and sensors used in AE9 (Electrons), AP9 (Protons) and SPM (Plasma). The columns from left to right give the satellite/sensor (see Appendix A for acronym definitions), approximate orbital parameters (perigee  $\times$  apogee, inclination), period from which data was taken and the energy range covered by the processed sensor data on the standard model grids. A \* indicates very sparse data coverage

Satellite/Sensor	Orbit	Temporal range	Energy range
Protons			(MeV)
CRRES/PROTEL	350 km $\times$ 33000 km, 18°	07/1990–10/1991	2.0–80
S3-3/Telescope	236 km $\times$ 8048 km, 97.5°	07/1976–07/1979	0.1–2.0
HEO-F1/Dosimeter	500 km $\times$ 39000 km, 63°	05/1994–02/2011*	10–400
HEO-F3/Dosimeter	500 km $\times$ 39000 km, 63°	11/1997–02/2011	10–400
ICO/Dosimeter	1000 km circular, 45°	06/2001–12/2009	10–400
TSX5/CEASE	410 km $\times$ 1710 km, 69°	06/2001–07/2006	10–400
POLAR/IPS	5100 km $\times$ 51000 km, 86°	02/1996–04/2008	0.1–1.0
POLAR/HISTp	5100 km $\times$ 51000 km, 86°	02/1996–04/2008	6.0–15.0
Electrons			(MeV)
CRRES/MEA/HEEF	350 km $\times$ 33000 km, 18°	07/1990–10/1991	0.1–7.0
SCATHA/SC3	28000 km $\times$ 43000 km, 7.8°	01/1979–05/1991	0.25–4.5
HEO-F1/Dos/Tel	500 km $\times$ 39000 km, 63°	05/1994–02/2011*	1.5–10.0
HEO-F3/Dos/Tel	500 km $\times$ 39000 km, 63°	11/1997–02/2011	0.5–5.0
ICO/Dosimeter	1000 km circular, 45°	06/2001–12/2009	1.0–7.0
TSX5/CEASE	410 km $\times$ 1710 km, 69°	06/2001–07/2006	0.07–3.0
SAMPEX/PET	550 km $\times$ 675 km, 82°	08/1992–07/2004	2.0–3.5
POLAR/HISTe	5100 km $\times$ 51000 km, 86°	02/1996–04/2008	1.0–6.0
GPS/BDDII ns18	20200 km circular, 55°	01/1990–05/1994	0.25–1.0
GPS/BDDII ns24	20200 km circular, 55°	08/1991–12/2000	0.25–1.0
GPS/BDDII ns28	20200 km circular, 55°	05/1992–09/1996	0.25–1.0
GPS/BDDII ns33	20200 km circular, 55°	04/1996–05/2004	0.25–1.0
LANL-GEO/SOPA 1989-046	36000 km circular, 0°	09/1989–01/2008	0.05–1.5
LANL-GEO/SOPA 1990-095	36000 km circular, 0°	11/1990–11/2005	0.05–1.5
LANL-GEO/SOPA LANL-97A	36000 km circular, 0°	07/1997–01/2008	0.05–1.5
LANL-GEO/SOPA LANL-02A	36000 km circular, 0°	01/2002–01/2008	0.05–1.5
Plasma			(keV)
POLAR/CAMMICE/MICS	5100 km $\times$ 51000 km, 86°	03/1997–09/1999	1.2–1.64
POLAR/HYDRA	5100 km $\times$ 51000 km, 86°	03/1997–09/1999	1.0–40.0
LANL-GEO/MPA 1990-095	36000 km circular, 0°	11/1990–11/2005	1.0–63.0
LANL-GEO/MPA 1991-080	36000 km circular, 0°	11/1991–11/2004	1.0–63.0
LANL-GEO/MPA 1994-084	36000 km circular, 0°	12/1994–01/2008	1.0–63.0
LANL-GEO/MPA LANL-97A	36000 km circular, 0°	07/1997–01/2008	1.0–63.0

field of view pitch angle channels. Each interval is assigned a unique Universal Time (UT)  $t$  and geographic position  $\mathbf{x}$  and the set of  $(\mathbf{x}, t)$  over the entire mission forms the satellite ephemeris. An expanded satellite ephemeris to include  $K, \Phi, h_{min}, L_m$  and other reference grid coordinates is computed as described in Sect. 3 with  $(\mathbf{x}, t)$ , energy and local pitch angle used as input.

Flux maps, correlation matrices and other statistical quantities underlying the model (Sect. 5) are all computed from sets of unidirectional fluxes  $j$  ( $\# \text{ cm}^{-2} \text{ s}^{-1} \text{ MeV}^{-1} \text{ sr}^{-1}$ ) derived from the measurements of each satellite sensor tagged to the reference grid via the expanded ephemeris. The standard deviation of the natural logarithm of the flux  $d \ln j$  is used as the estimate of the uncertainty. Transformation of the typical raw sensor output, e.g. counts/sec, into an estimate of the differential flux with error occurs through an often lengthy process. Data cleaning, spectral inversion, angular mapping, interpolation and cross-calibration are essential components and their application is discussed in this section.

#### 4.1 Cleaning

During the course of a mission data from a given sensor can be corrupted due to a variety of issues including design imperfections, fabrication flaws, degradation of components, telemetry errors, background contamination and saturation. Some simple examination procedures can often be used to examine the entire data set and generate rules that define ranges of measurement values, regions of coordinate space or periods of time where the data is suspect and not to be used for model development. Such procedures are applied to the raw data before any sophisticated reduction algorithms (e.g. spectral inversion) which might obscure the problems. The procedures considered for the AE9/AP9/SPM data sets are extensions of those discussed in the PRBEM Data Analysis Procedure document (Bourdarie et al. 2008) and discussed in O'Brien (2012b). Included are (a) scatter plots of measurements in one channel (usually color-coded by time or coordinate, for example) against measurements of another correlated measurement channel such as an adjacent energy or pitch angle channel (identifies single channel problems of all sorts and contamination when the correlated channel is the protons in an electron dosimeter channel, for example); (b) scatter plots of measurements in one channel against measurements in the same channel offset in time (identifies transient spikes); and (c) histograms of the number of occurrences of every possible value of the raw measurement (identifies saturation and bit errors). It is also helpful to plot the data as a function of time for the entire mission with different coordinates color-coded to identify potential time-dependent sensor degradation.

All of the data sets in AE9/AP9/SPM were cleaned with at least one of the procedures and in many cases (e.g. the dosimeters) several of them. Ultimately it is the judgment of the analyst as to how to generate rules on which points to exclude; however, in most cases there are clear anomalies unambiguously associated with certain spatial regions, temporal periods or background flux levels. Once the rules were generated, a new data set for each sensor was created with flags to indicate the bad measurements to be rejected in further analysis.

For the CRRES/PROTEL proton data an explicit background contamination correction was implemented similar to that done by Gussenhoven et al. (1993) but in  $(K, h_{min})$  coordinates instead of  $(L_m, B/B_0)$  coordinates. Unlike the cleaning procedures mentioned above, which simply remove bad points from further analysis, the contamination correction goes further and corrects measured values based on an estimated background. At each measurement interval the  $(K, h_{min})$  values are computed for all measured pitch angles. The flux value of the first pitch angle bin with  $h_{min} < 100$  km (a nominal altitude within the loss cone where the trapped proton flux is zero) is then subtracted from the flux values of all bins with  $h_{min} > 100$  km (the correction) and the entire set of flux values for  $h_{min} < 100$  km is set equal to zero (the cleaning). Corrections were significant only within the inner zone  $L^* < 1.7$  and the resulting flux maps were insensitive to different methods for estimating the loss cone.

The CRRES/HEEF and CRRES/MEA sensor data provide a unique LEO-to-GEO view of the trapped energetic electrons and are important in the development of AE9. Both sensors

have been analyzed in some detail (e.g. Hanser 1995; Dichter et al. 1993; Cayton 2007 and Vampola 1996) and the data is found in other models, e.g. CRRESELE. Significant additional work was done for AE9 to include more extensive proton contamination removal, spectral correction of MEA data and adjustment of HEEF data at high flux levels (Johnston et al. 2011).

## 4.2 Spectral Inversion and Pitch-Angle Mapping

It is straightforward to assign flux measurements made by sophisticated particle detectors with high spectral and pitch angle resolution (e.g. CRRES/PROTEL and POLAR/HISTp) to specific ( $E$ ,  $K$ ,  $\Phi$  or  $h_{min}$ ) bins by simple interpolation, usually of the log of the flux. These types of detectors are relatively few and far between, however, and spatial and temporal coverage of the radiation belts can be expanded considerably by using measurements from dosimeters. With wide fields-of-view and relatively small numbers of integral energy channels, dosimeters produce data that require a substantial amount of processing in order to assign a unidirectional flux value to a reference grid bin. Sensors listed in Table 3 falling into this category are the ICO/Dosimeter, the HEO-F1/Dosimeter, the HEO-F3/Dosimeter, the TSX5/CEASE dosimeter and broad-channel particle telescope, the LANL-GEO/SOPA telescopes and the GPS/BDDII dosimeters. Given the extensive use of dosimeter data sets in V1.0 and the uniqueness of the processing methods as applied to radiation belt models a brief description is given here.

Converting the measured counts/sec  $C_i$  in  $i = 1, \dots, N$  dosimeter channels into unidirectional flux  $j$  involves inverting in some manner the following relation (e.g. Sullivan 1971),

$$C_i = \int_0^\infty dE \int_0^{2\pi} d\varphi \int_0^\pi d\theta \sin\theta \varepsilon_i(E) A_i(E; \theta) j(E; \theta, \varphi), \quad (4)$$

where  $(\theta, \varphi)$  are spherical coordinate angles describing the field of view in the frame where the  $z$  axis is along the detector bore sight,  $\varepsilon_i(E)$  is the detector efficiency and  $A_i(E, \theta)$  is the effective area of the detector channel assuming symmetry in azimuth. For V1.0 a two-step process was employed separating out the spectral inversion and angular mapping parts.

First, the flux was assumed to be isotropic, i.e.  $\bar{j}(E) = j(E, \theta, \varphi)$ , and was obtained using standard non-linear optimization techniques (cf. Press et al. 1992; O'Brien 2010) from the angular integrated form of Eq. (4),

$$C_i = \int_0^\infty dE R_i(E) \bar{j}(E), \quad (5)$$

where  $R_i(E)$  is the known channel response function defined as,

$$R_i(E) = 2\pi \int_0^\pi d\theta \sin\theta \varepsilon_i(E) A_i(E; \theta). \quad (6)$$

Detailed response function models based on Monte-Carlo simulations of energy deposition in materials were available for the TSX5/CEASE (Brautigam et al. 2006) and LANL-GEO/SOPA (Cayton and Belian 2007) sensors. Accurate geometric factors were also measured prior to launch for the electron response of the HEO and ICO dosimeters. Such information was not available for the proton response of the ICO and HEO dosimeters, and an alternative method to determine the geometric factors was developed using on-orbit observations of solar proton events and inter-calibration with GOES/SEM observations (Guild et al. 2009). Principal component analysis was used to *a-priori* parameterize the spectral shapes by generating  $L^*$ -dependent basis components derived from the Selesnick Inner Zone Model

for protons (Selesnick et al. 2007) and the CRRES/HEEF/MEA data for electrons (Johnston et al. 2010). In the LANL-GEO/SOPA analysis a double relativistic Maxwellian was assumed as the parameterized spectral function.

For the GPS/BDDII, the flux conversion factors were determined through a cross-calibration analysis with CRRES/MEA data (Friedel et al. 2005). Gain settings for each channel were varied as a function of time throughout the mission to maximize the count statistics. This changed the channel energy threshold and consequently a set of fixed ‘virtual’ energy channels was created through interpolation for use in AE9.

A second step of angular mapping is needed to estimate a value for the locally-mirroring unidirectional flux  $j_{90}$  from the measurements made over the wide fields-of-view characteristic of the dosimeters. This was accomplished by finding the value of  $j_{90}$  which best generates the measured flux using an *a-priori* model for the local pitch angle distribution. Electron pitch-angle distributions were modeled using the work of Vampola (1996) based on the CRRES/MEA data. Proton pitch-angle distributions were taken from the CRRESPRO model (Meffert and Gussenoven 1994) with East-West effect directionality corrections applied to the TSX5/CEASE data using the model of Lenchek and Singer (1962). For the HEO, ICO and GPS sensors the look direction of the detector was not known and therefore assumed to be random. Look direction information was available for CEASE/TSX5 and consequently a more accurate mapping to  $j_{90}$  was obtained.

After the inversion process is complete the net result for a single measurement interval is the flux amplitude  $j_{90}(E, K, \Phi)$  or  $h_{min}$ ) where the value of  $K$  corresponds to locally mirroring particles, and  $E$  spans the range of standard energy bins where the spectral inversion is valid. Also output is the standard deviation  $d \ln j$  which combines the errors of the spectral inversion and angular determination processes. Note that the uncertainty of the initial measurements (Sect. 4.3) is an input to the spectral inversion algorithm. In principle algorithms could be developed which, given knowledge of  $A_i$  and the look direction, determine  $j$  from the known count rates by simultaneously optimizing over both the  $E$  and  $\theta$  coordinates. In LEO, where pitch-angle distributions can be sharply peaked, the combined inversion is very sensitive to the pitch-angle distribution models and successful implementation awaits more accurate characterization.

A different angle determination problem arises with the LANL-GEO/SOPA and MPA sensors. Though these sensors have relatively good angular resolution, the LANL-GEO satellites on which they are situated do not have magnetometers. Pitch-angle determination must be made with algorithms which exploit the asymmetries observed in the different angular bins over the course of a spin period (Chen et al. 2005; Thomsen et al. 1996). Not all LANL-GEO satellite data sets have been processed yet to yield the pitch-angle resolved data thereby limiting the data sets available for V1.0 to those listed in Table 3.

#### 4.3 Cross-Calibration

Flux measurements exhibit considerable uncertainty due to a wide variety of effects including imperfect sensor electronics, materials degradation, contamination, inadequate calibration and error in spacecraft location, orientation and magnetic environment. Deriving an error budget for each sensor from a detailed bottom-up analysis is an impossible task in most cases. The response of key detector elements was often never measured or recorded, and detailed performance models are rare. Instead, for AE9/AP9/SPM errors were estimated using an on-orbit cross-calibration technique whereby the data from two sensors nominally measuring the same environment (a “conjunction event”) were compared, the average bias determined and the residual error (after removing the bias) computed. Starting, for each

species, with a “reference sensor” deemed to be the most accurate (call this sensor A) the data from a sensor (Sensor B) cross-calibrated with A was adjusted by the bias value and the residual error in the natural log of the flux was assigned as the variance for Sensor A and Sensor B. The next sensor in the chain (Sensor C) was cross-calibrated with Sensor B, and the error assigned to Sensor C was the residual between B and C. A bias was then assigned to Sensor C equal to the product of the A-B and B-C biases so as to put the Sensor C measurements on the same level, on average, as Sensor A. Progressing through a series of conjunction events, as described below, all the sensors were compared and corrected. Data sets of  $j$  ( $E, K, \Phi$  or  $h_{min}$ ) with errors  $d \ln j$  were derived for each sensor as inputs to the flux map process (Sect. 5.1). There were a few sensor data sets where conjunctions did not exist with other sensors, e.g. S3-3/TEL, in which case a self-calibration was performed using sequential revisits to the same region of phase space to estimate the error with no applied bias corrections. The cross-calibration technique is an extension of Friedel et al.’s (2005) method with the addition of the residual error.

Prior to this inter-comparison the sensor data was processed at the lowest level required to produce a meaningful result. Differential energy channels on one sensor were sometimes summed and interpolated to produce matches with another sensor with different energy channel values or integral response channels. Detailed pitch-angle data was spin-averaged to estimate omni-directional fluxes which were used for comparison. Channels were combined so that for a given sensor-to-sensor pairing the manipulation was done, to the extent possible, on the most accurate sensor to reconstruct the energy channel on the least accurate sensor. Dosimeter channels were compared using geometric factor approximations of the response to turn count rates into integral fluxes, rather than the more complex spectral inversion that was performed after the measurement uncertainties were estimated (Sect. 4.2).

Solar particle events (SPEs) simplify cross-calibration of the proton sensors by providing a relatively homogeneous environment in LEO, HEO, MEO and GEO, at least at high latitudes and altitudes. Conjunction events were defined as the simultaneous observation of an SPE by more than one sensor. The reference sensor was taken to be the much-studied GOES/SEM detector (GOES I-M 1996) with a correction made to the differential energy values assigned to the published channel values to better account for the monotonically decreasing spectra across the channel bins (Ginet et al. 2010). Figure 2 summarizes the cross-calibration chain for the proton data used in V1.0. Data from the sensors GOES7/SEM, GOES8/SEM, GOES11/SEM, ACE/EPAM and IMP8/CPME were crucial for SPE cross-calibration but were not used in the model since all were outside the region of trapped energetic protons. S3-3/TEL was self-calibrated since it measured the low proton energy range ( $\sim 0.1\text{--}2$  MeV) not adequately covered by the GOES/SEM sensor. Similar low energy coverage restrictions apply to the POLAR/IPS sensor but conveniently the ACE/EPAM sensor was available during the POLAR mission to enable cross-calibration during SPEs.

Since there does not exist the equivalent of SPEs bathing the entire high- $L$  shell magnetosphere in a relatively uniform flux of energetic electrons for extended periods of time, the cross-calibration of the electron sensors has to be done through magnetic conjunctions (Friedel et al. 2005). Measurements from two sensors are compared when they are made in close magnetic proximity at the same time, i.e. the  $\Delta L_m$ ,  $\Delta B/B_0$ ,  $\Delta MLT$  and  $\Delta t$  between the sensors are all small, where MLT is the magnetic local time, and the conjunction occurs in a period of magnetic stability, i.e.  $K_p < 2$  for an extended period of time preceding the measurement, where  $K_p$  is the planetary magnetic index. In reality, the exact values defining the small  $\Delta$  criteria have to be adjusted on a case-by-case basis in order to maintain a statistically significant number of comparison points. Typical values chosen were  $\Delta L_m < 0.1$ ,  $\Delta B/B_0 < 0.1$  and  $\Delta t < 4$  hours with measurements made between 4:00

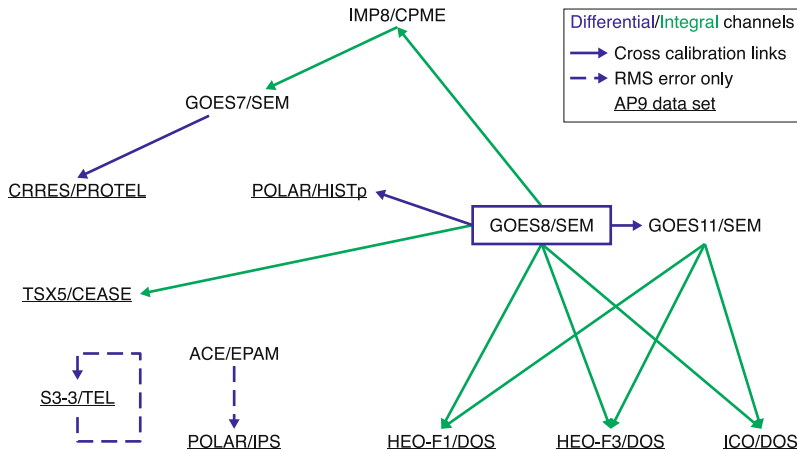


**Fig. 2** Cross-calibration chain for the proton data sets in AP9. The *blue box* encloses the reference satellite/sensor data set, while satellite/sensor data sets included in the model are underlined. *Solid blue* and *green lines* are differential and integral channel comparisons, respectively, and *dotted lines* represent RMS error determination only

$< \text{MLT} < 8:00$  (dawn) or  $16:00 < \text{MLT} < 20:00$  (dusk) with  $K_p < 2$  for the prior 48 hours. The reference sensor was taken to be the combined CRRES/HEEF and CRRES/MEA data set given its broad  $L$ -shell coverage and the extensive work that has been done trying to understand the response and correct for contamination (Sect. 4.1). Figure 3 shows the chain of calibration employed in V1.0 for the energetic electron sensors. The choice of conjunctions is not unique in that a single satellite could have conjunctions with several others. In these cases the conjunctions having the most points were used, which were usually the ones giving the best agreement over the entire spectrum. SAMPEX/PET was self-calibrated because even though there were conjunction events with TSX5/CEASE, SAMPEX/PET was a much more accurate sensor requiring no error-inducing spectral inversion.

The cross-calibration chains for plasma ions and electrons are illustrated in Fig. 4. No bias corrections were applied since the observed differences between LANL-GEO/MPA series were small and the residuals between the POLAR sensors and LANL-GEO/MPA were much larger than the bias. Two versions of the POLAR/CAMMICE/MICS data were used, the first from Roeder et al. (2005) and the second from Niehof (2011). Different processing methods were used which yielded flux estimates that were not always in agreement. Since it was not clear which method was superior, both data sets were used as independent inputs to the flux map building routine (Sect. 5.1) where the bootstrapping algorithm melded the uncertainties.

## 5 Architecture

### 5.1 Flux Maps

Underlying AE9/AP9/SPM is a set of empirical flux maps constructed from the collection of multi-satellite differential flux measurements cleaned, cross-calibrated and sorted into reference grid bins as described in the previous sections. Maps are made for two statistical quantities: the 50th (median) and 95th percentile flux values in each reference grid bin, hereafter

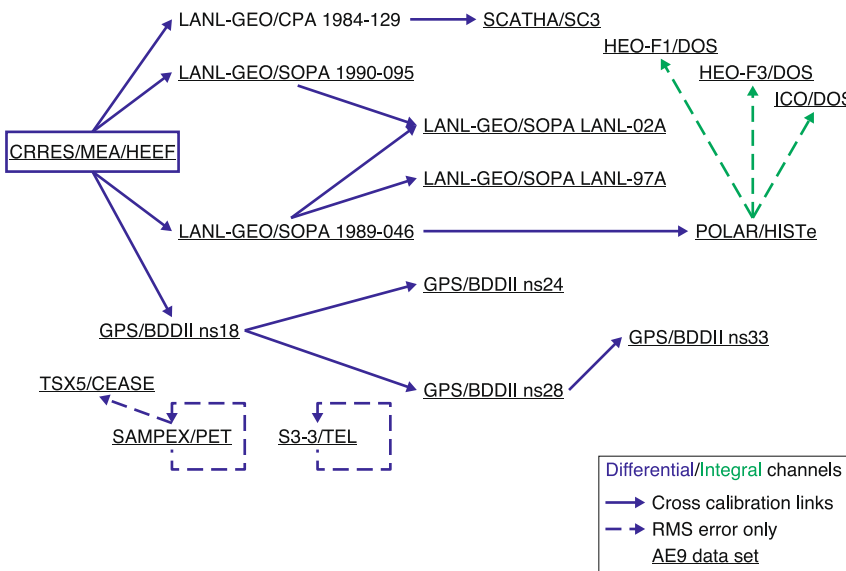


**Fig. 3** Cross-calibration chain for the electron data sets in AE9. See Fig. 2 caption for a description

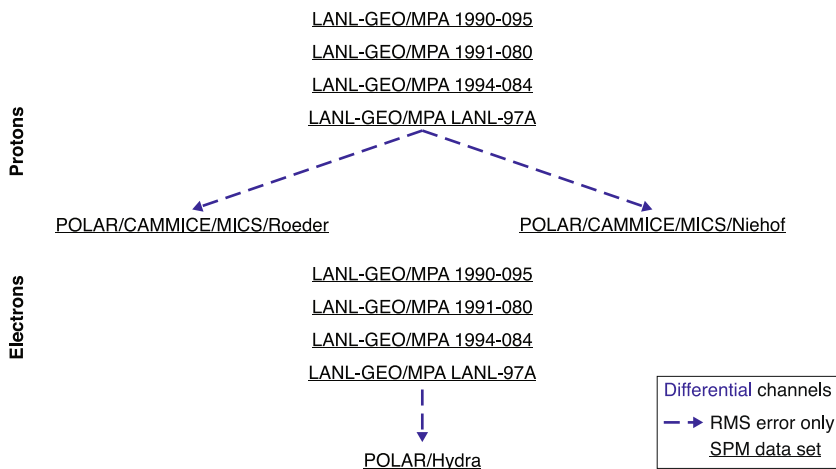


**Fig. 4** Cross-calibration chain for the plasma data sets in SPM. See Fig. 2 caption for a description

labeled  $m_{50}$  and  $m_{95}$ , respectively, or together as the vector  $\underline{\theta} = (m_{50}, m_{95})$ . An estimate of the uncertainty  $\delta\underline{\theta}$  in each bin is also made. The map generation procedure is illustrated on the left-hand side of Fig. 5 and described in some detail in Appendix B. Both uncertainty in measurement and space weather give rise to the spread of the distribution as quantified by  $\underline{\theta}$ . Even if the measurements were perfect there would still be a difference between  $m_{95}$  and  $m_{50}$  due to the natural variations caused by geomagnetic storms, atmospheric heating, co-rotating interaction regions, and other space weather effects over the course of the solar cycle. These variations are implicitly captured in the model by independently tracking flux values corresponding to these two percentiles.

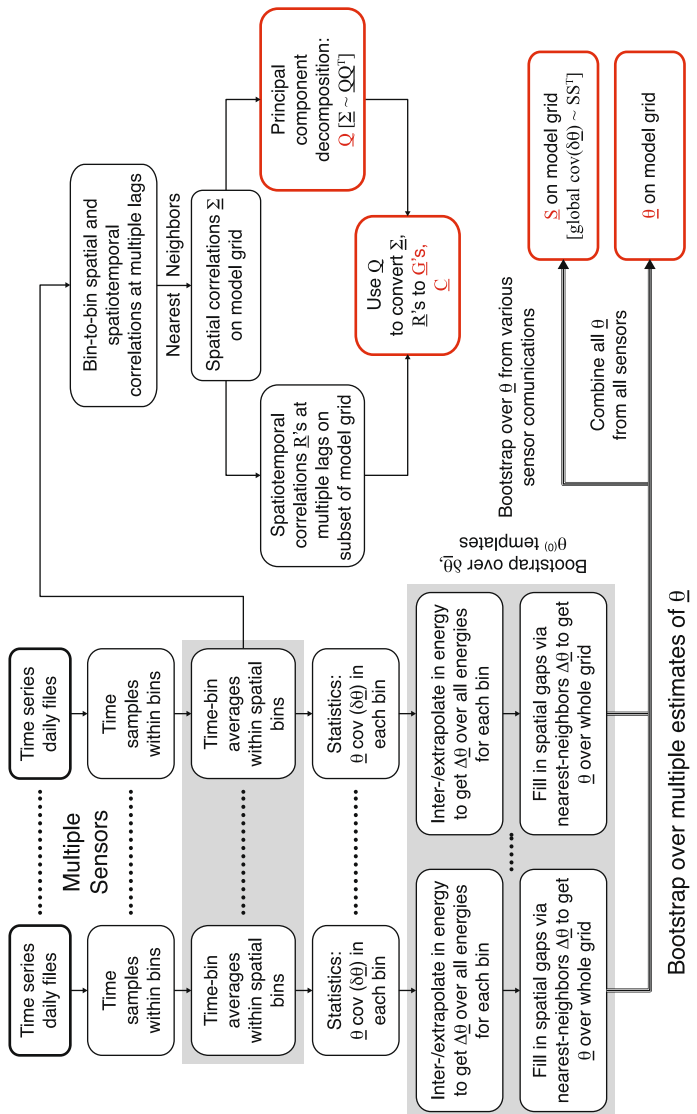


**Fig. 5** Schematic of the processes for building the flux map (*left side*) and spatiotemporal covariance matrices (*right side*). See Sect. 5 and Appendix B for details

**Table 4** Sources for templates used in developing AE9, AP9, and SPM

AE9	AP9	SPM
<ul style="list-style-type: none"> <li>• AE8 profiles</li> <li>• CRRES/MEA + HEEF</li> </ul>	<ul style="list-style-type: none"> <li>• S3-3/TEL + CRRES/PROTEL + TSX5/CEASE (<math>K - h_{min}</math> grid)</li> <li>• POLAR/IPS + CRRES/PROTEL + TSX5/CEASE (<math>K - \Phi</math> grid)</li> </ul>	<ul style="list-style-type: none"> <li>• POLAR/CAMMICE/ROEDER + POLAR/CAMMICE/NIEHOF data (ions)</li> <li>• Milillo model (Milillo et al. 2001) (ions)</li> <li>• POLAR/HYDRA (electrons)</li> </ul>

Two elements are crucial for map building: bootstrapping and gap-filling. The former process is a well-established technique whereby statistical quantities (e.g.  $\underline{\theta}$ ) are computed by re-sampling with replacement from the observed sample (e.g. Efron and Tibshirani 1993). Besides an estimate for the quantity itself, bootstrapping provides an estimate for the standard deviation of the quantity (e.g.  $\delta\underline{\theta}$ ) and is very useful in “rolling up” uncertainties at lower levels of the analysis (e.g. uncertainties in the flux values, interpolation algorithms, etc.) when applied properly.

For the gap-filling process a template technique is employed. Templates are defined as *a-priori* estimates of the shape of the  $\underline{\theta}$  dependence on the model coordinates derived from the examination of data sets, physics-based modeling and the judgment of an experienced space physicist. There is not a single best template for each species, rather, there are a variety of templates characterizing different dynamic states of the radiation belts. As an extreme example, the distributions of energetic protons and electrons in the slot region look much different before and after the March 1991 geomagnetic storm (Brautigam et al. 1992; Gussenhoven et al. 1993). In V1.0 a number of templates were created by team members based on different combinations of data sets and models as summarized in Table 4. Full reference grid maps for each satellite data set are obtained by using the templates and applying bootstrapping techniques (Appendix B) to capture both the uncertainty in the measurements and that arising from non-unique templates. Templates are very much an art involving data, experience and intuition. More diverse and hopefully accurate templates can easily be accommodated in future builds of the model.

Transforming the maps of the percentile values and associated uncertainties into maps of flux  $j$  and uncertainty  $d \ln j$  requires the choice of a two-parameter distribution function for each species. Examination of the data from some of the higher resolution sensors (e.g. CRRES/HEEF, CRRES/PROTEL and LANL/MPA) indicates that the Weibull distribution (O’Brien and Guild 2010) is a reasonable choice for the electrons and the lognormal distribution (Evans et al. 2000) is satisfactory for the energetic protons and plasmas. Armed with the functional form of the distribution function the values of ( $m_{50}$ ,  $m_{95}$ ) in each reference grid bin can be readily translated into a distribution of  $j$ . At this point the model already provides a capability to the user superior to existing models: a map of the flux distribution on the reference grid with an estimate of measurement and mapping uncertainties. Many recalculations of the  $j$  distribution using values of  $\underline{\theta}$  randomly perturbed by a small amount consist with the deviation  $\delta\underline{\theta}$  provide estimates of the uncertainty in  $j$ , or any quantity computable from  $j$ , arising from the imperfect measurements, data processing and mapping processes.

## 5.2 Time Evolution

To model variations of the flux on time scales less than a solar cycle an auto-regressive time-evolution model has been developed. The dynamics are governed by the relation,

$$\mathbf{q}(t) = \sum_{k=1}^{N_G} \mathbf{G}_k \mathbf{q}(t - \tau_k) + \mathbf{C} \boldsymbol{\eta}(t), \quad (7)$$

where  $\mathbf{q}$  represents the principal component amplitudes of the spatial variation of the flux over the reference grid,  $\mathbf{G}_k$  is the time evolution matrix defined for  $k = 1$  to  $N_G$  specific time lags  $\tau_k$  and  $\mathbf{C}$  is the “innovation” term allocating the white-noise driver to the principal components. The right-hand side of Fig. 5 schematically illustrates how the aforementioned vectors and matrices are constructed from the satellite flux data and Appendix B delves into the details. Suffice it to say that a map of the flux  $j$  at time  $t$  on the reference grid is uniquely determined by the principal component  $\mathbf{q}(t)$ , the values of the percentile flux map  $\underline{\theta}$  and the choice of distribution function. A random but statistically realistic time-history of flux can be generated from Eq. (7) by choosing a random number seed at  $t = 0$  which generates the initial principal component amplitudes  $\mathbf{q}(0)$  and the percentile parameters  $\underline{\theta}$  constrained by the uncertainty  $\delta\underline{\theta}$ .

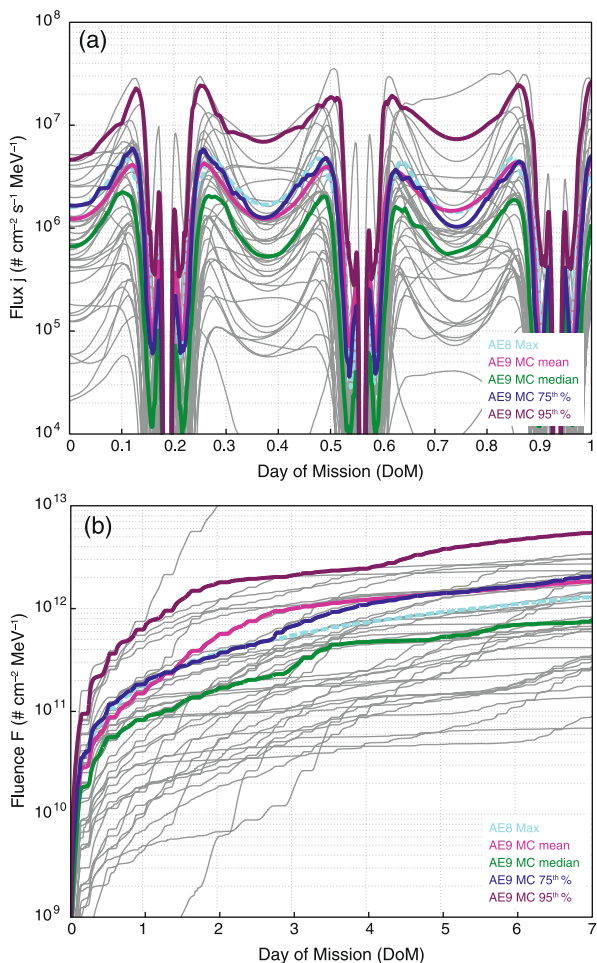
For AE9  $N_G = 6$  and for AP9  $N_G = 4$  with the time lags chosen to be 1 day (electrons only), 1 week, 2 weeks (electrons only), 27 days, 6 months and 1 year, i.e. values that capture geomagnetic storm (albeit at low-resolution), solar rotation, seasonal and solar cycle space weather variations. There is no solar-cycle phase dependence in the model, i.e. statistics are computed from all of the data sets independent of phase. The reasoning behind this is (a) missions often last longer than a solar cycle, (b) launch dates are often uncertain in the design phase and (c) solar activity is notoriously unpredictable on solar-cycle time scales. It would simply not be prudent for an engineer to design to a particular phase of the solar cycle. As mentioned in Sect. 3, the plasma models do not contain a dynamic component because an adequate description involves time scales (minutes) and spatial coordinates (MLT) requiring a more sophisticated analysis than undertaken for V1.0.

## 5.3 Application

The primary functionality of AE9/AP9/SPM is a “fly-in” software function. A user inputs the satellite ephemeris, energy range of interest, model selection and “specification mode” and is returned a time series of the flux values for the requested energy channels along the orbit. There are three specification modes delineated by the method by which the flux values are determined in each coordinate bin along the orbit: (a) mean—using only the average values for  $\underline{\theta}$  to compute the mean flux in each reference grid bin; (b) perturbed mean—using the average  $\underline{\theta}$  plus a random perturbation consistent with  $\delta\underline{\theta}$  to compute the mean flux in each bin and (c) full Monte-Carlo using the autoregressive time-evolution model with a random initial condition  $\mathbf{q}$  and perturbed  $\underline{\theta}$  for flux conversion. The mean fly-in mode captures the mean behavior of the model with no uncertainty added while the perturbed mean adds the uncertainty in the flux maps due to measurement and gap-filling errors. A full Monte-Carlo run contains all of the perturbed mean uncertainty plus an estimate of the dynamic variations due to space weather processes.

Meaningful information on average or worst cases fluxes and percentile levels can be derived from multiple applications of the fly-in routines in either perturbed mean or Monte-Carlo mode. By aggregating the results of a large number of mission scenarios, each scenario run with the same ephemeris but with a different random number seed, the percentile flux

**Fig. 6** Flux profiles of  $>1$  MeV electrons from AE9. Light grey lines are individual MC scenarios and the mean, median, 75th and 95th percentile aggregates are the pink, green, blue and maroon lines, respectively. AE8 MAX as shown as the light blue dotted line



levels of any quantity derivable from the flux spectrum, e.g. fluence (time integrated flux) or total dose, can now be specified in terms of probabilities of occurrence during the course of the mission. Dose calculations require, of course, a code such as SHIELDOSE-2 (Seltzer 1994) that takes flux as input and outputs energy deposited in various materials behind user-defined Aluminum shielding thicknesses. An example of aggregation is given in Fig. 6 where the time profiles of the 1 MeV electron flux and fluence as output by AE9 are plotted for 40 Monte-Carlo scenarios (grey lines) run for a geosynchronous transfer orbit. The aggregated mean (pink), median (green), 75th percentile (blue) and 95th percentile (maroon) are shown as well as the output from AE8 MAX (light blue) for comparison. More examples will be discussed in Sect. 5.

The fly-in function in V1.0 is provided by a C++ object with wrappers available in C and Fortran. An application tool has also been built by the AE9/AP9/SPM team which provides an orbit propagator, scenario generator and aggregator for sets of perturbed mean and Monte-Carlo runs. It is accessible by both a command line and graphical user interface. Output is in the form of simple plot and text files. The SHIELDOSE-2 application is included as well as the historical AE8/AP8 (Sawyer and Vette 1976; Vette 1991b),

**Table 5** Computer runtimes for AP9/AE9/SPM V1.0 in mean, perturbed mean (40 scenarios) and Monte-Carlo (40 scenarios) modes covering different orbit regimes. Benchmarks were done on a standard desktop 3.4 GHz Intel Core i7-2600 CPU

Orbit	Time step (sec)	Run time (minutes)					
		1 day mission			1 year mission		
		Mean	Pert. Mean (40 Scenarios)	Monte-Carlo (40 scenarios)	Mean	Pert. Mean (40 Scenarios)	Monte-Carlo (40 Scenarios)
GEO	3600	6.7E-03	1.7E-02	1.4E-01	2.5E+00	6.2E+00	4.9E+01
MEO	300	8.1E-02	2.0E-01	1.6E+00	3.0E+01	7.4E+01	5.9E+02
HEO	60	4.0E-01	1.0E+00	8.1E+00	1.5E+02	3.7E+02	3.0E+03
LEO	10	2.4E+00	6.1E+00	4.9E+01	8.9E+02	2.2E+03	1.8E+04

CRRESELE (Brautigam and Bell 1995), CRRESPRO (Meffert and Gussenoven 1994) and CAMMICE/MICS (Roeder et al. 2005) models. Plans are underway to ultimately host the project on an open source repository to facilitate broad collaboration.

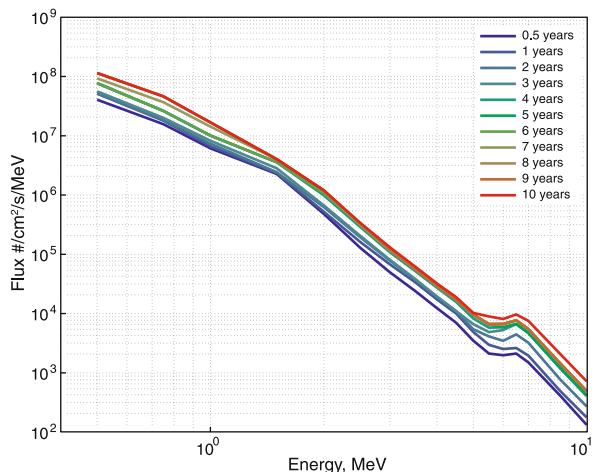
## 6 Verification and Validation

Verification and validation are essential for any model aspiring to be an engineering application. That is, the model must run according to design and produce results consistent with independent data. These steps are especially important for AE9/AP9/SPM given the uniqueness and complexity of the algorithms and the diversity of the data sets.

With any Monte-Carlo (MC) type model, the statistics always improve with the number of runs performed. In testing V1.0 each perturbed mean or MC demonstration consists of 40 scenarios. Though somewhat arbitrary, this number is computationally realizable (see below) and dictates that the scenario with the 2nd largest magnitude defines the 95th percentile. The primary test suite runs the full set of models AE9, AP9, SPMH, SPMHE, SPMO and SPME in mean, perturbed mean and MC (where applicable) modes for 8 different orbits to include 3 in LEO (400 km, 800 km and 1200 km, circular, 90° inclination), GTO (500 km × 30600 km, 10° inclination), HEO (1475 km × 38900 km, 63.4° inclination), MEO (3900 km × 14100 km, 120° inclination), GPS (20200 km, circular, 55.0° inclination) and GEO (35786 km, circular, 0° inclination). The mission time was taken to be one week, certainly shorter than a typical real-world mission but long enough to observe the dynamic effects in the model. Several examples from the test suite will be presented in Sect. 6.1 and compared with historical data. Other runs were done for much longer periods and are compared to data in Sect. 6.2. As might be expected, execution of the test suite uncovered a number of data set and algorithm issues, many which have been fixed but some which have not (Sect. 7).

As might be expected, the full Monte-Carlo execution of many AP9 and AE9 scenarios for multi-year missions in certain orbits can lead to fairly large computational times. Table 5 displays a representative set of computer run times for V1.0 in various modes derived from the test suite and benchmarked on a typical high-end desktop computer circa 2011 (specifically one with a 3.40 GHz Intel Core i7-2600 CPU). The time steps were chosen to ensure that the spatial structures and temporal variation of the belts in each orbit regime are adequately sampled. Time steps larger than these risk undersampling the flux spatial structure. Summarizing the far right-hand column in units of hours and days a 1 year mission at

**Fig. 7** Spectra of the 95th percentile 24 hour averaged electron flux along a HEO orbit for different mission simulation periods ranging from 0.5–10 years (see key). All simulations comprised 40 MC runs



GEO, MEO, HEO and LEO can be run in 0.8 h, 10 h, 2.1 days and 12.8 days, respectively. Run times can be large, especially when considering a 10 year mission in LEO, but the MC processing can easily be split onto a large number of machines. Unfortunately, a 10 year mission does have to be simulated for the full 10 years because the 11-year solar cycle driving space weather imparts substantial dynamical variations on long time scales and these are statistically captured in the model. Figure 7 illustrates this by showing a spectrum of the 95th percentile, one-hour averaged electron flux along a HEO orbit computed for mission durations ranging from 0.5–10 years with 40 MC scenarios for each mission. Worst case values (e.g. the 95th percentile of the 24 hour average) do not necessarily converge, even after 10 years, but long term averages (not shown) do converge to the perturbed mean.

### 6.1 Comparison to Models

Outputs from the AE9 Monte-Carlo (MC) runs at GEO are shown in Fig. 8 to include a time history of the 2 MeV flux (Fig. 8a) over the course of 2 days, a time history of the 2 MeV fluence over the course of 7 days (Fig. 8b), the 7 day fluence spectra for the AE9 mean with output from historical models (Fig. 8c) and the 7 day fluence spectra for the entire set of MC scenarios (Fig. 8d). In Figs. 8a, 8b and 8d each grey curve represents one of the 40 MC scenarios and the pink, green, blue and maroon curves represent the aggregated mean, median, 75th and 95th percentile, respectively. The AE8 MAX prediction is shown as the dotted light-blue curves in all panels of Fig. 8. Predictions from the CRRESELE average model (Brautigam and Bell 1995) and the combination of the LANL-2007 plasma model (Thomsen et al. 2007) and the IGE-2006 energetic electron model (Sicard-Piet et al. 2008) are shown in Fig. 8c.

It is clear that AE9 indicates significant uncertainty in the levels of energetic electrons at GEO as demonstrated by the wide spread in the MC scenario runs. This is not surprising, since this population is known to be highly variable at GEO, existing at the whim of dynamic processes in the plasma sheet and the impact of high-speed solar wind streams. The amplitude of the spectra for the AE9 mean is often higher than the historic models (Fig. 8c) though the median value is in closer agreement and all the models are within the uncertainty of the 40 MC scenarios (Fig. 8d). There can also be differences between the historical models of similar or greater magnitude than their disagreement with AE9.

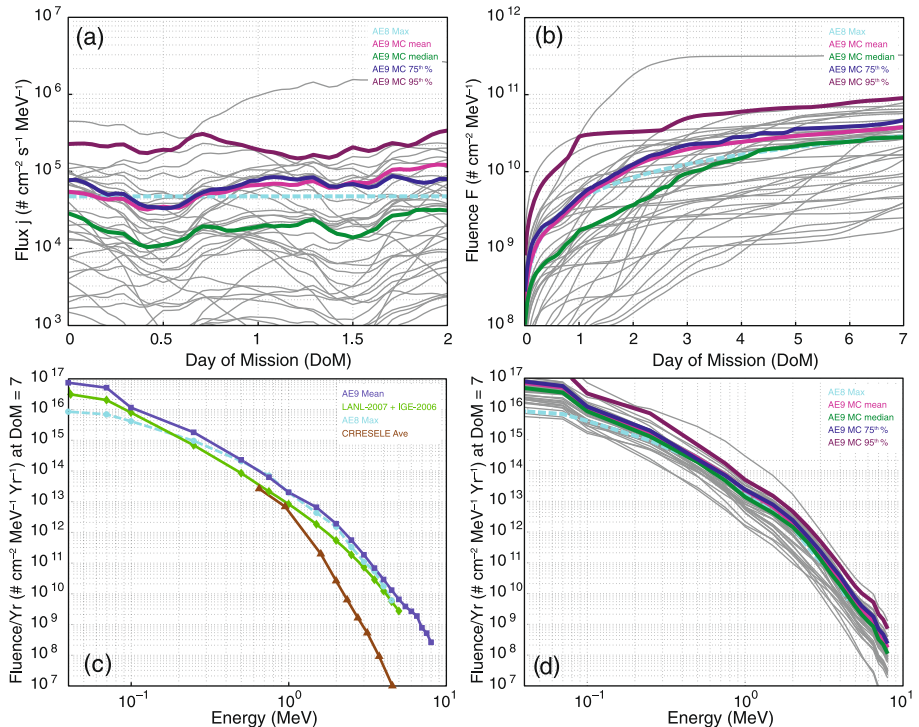


**Fig. 8** Flux (a) and fluence (b) histories of  $>2$  MeV electrons in GEO from AE9. Light grey lines are individual MC scenarios and the mean, median, 75th and 95th percentile aggregates are the pink, green, blue and maroon lines, respectively. Output from AE8 MAX is shown as the light blue dotted line. Shown in (c) is the fluence spectra after 7 days from the AE9 median (dark blue), AE8 MAX (light blue), CRRESELE Average (brown) and the LANL-2007—IGE (green) models. The full set of 7 day MC fluence spectra is shown in (d) with the same color convention as (a)

Figure 9 shows time series and spectra relevant to 20 MeV protons for the 800 km LEO orbit as specified by AP9. The format is the same as in Fig. 8 but the comparison models are now AP8 MAX and CRRESPRO Active (Meffert and Gussenhenven 1994) and the span of the flux time series is limited to 0.2 days to better observe the passage through the South Atlantic Anomaly (SAA). Values of the AP9 mean are well above AP8 and closer to CRRESPRO except at the highest energies. Both historical models are within the 40 MC scenario uncertainty except for energies greater than  $\sim 25\text{--}40$  MeV where CRRESPRO is smaller and AP8 is larger than AP9. The tendency for AP8 to predict lower proton fluxes than what is measured in LEO has been noted previously (e.g. Huston 2002; Ginet et al. 2007).

The results of running the SPMH model for a GPS orbit are shown in Fig. 10 using the same format as Fig. 8 but with a 1 day duration for the flux versus time profile. Here CAMMICE/MICS (Roeder et al. 2005) is the historical model for comparison. The fluence spectra of CAMMICE/MICS is 2–3 times smaller than the SPMH mean (Fig. 10c) and does not appear to be within the uncertainty. However, in the data reduction process the error in SPMH has been clamped to a relatively small value to eliminate the unrealistically large swings in spectral shape that were manifest if the empirical uncertainties were used. Such large empirical uncertainties and the necessity to artificially suppress them should disappear

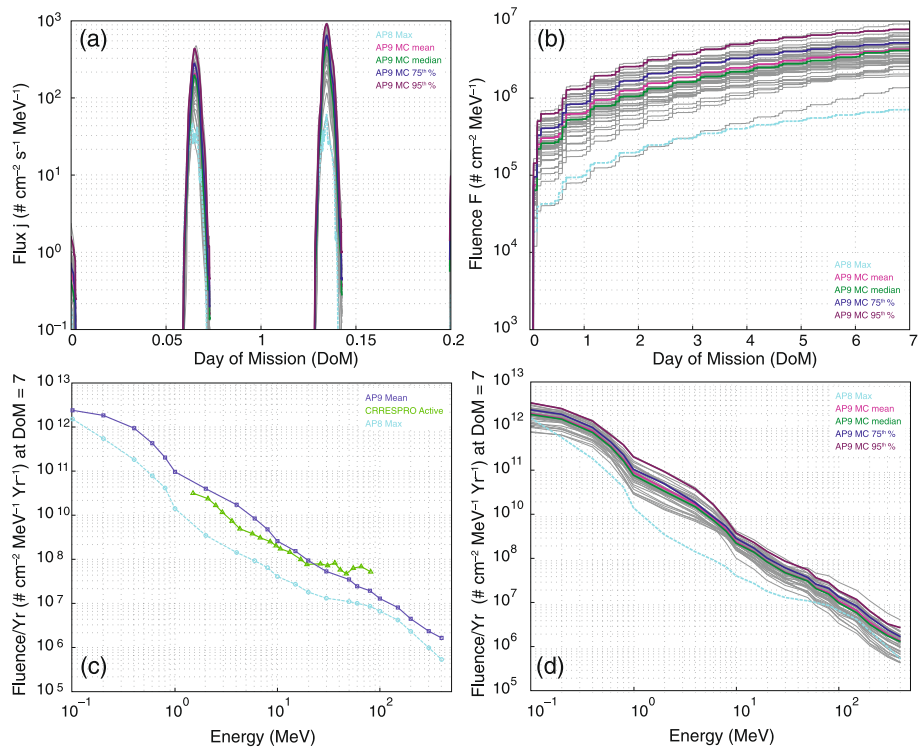


**Fig. 9** Flux (a) and fluence (b) histories of  $>20$  MeV protons in LEO (800 km) from AP9. See Fig. 8 caption for the color convention. AP8 MAX model predictions are shown as the *light blue dotted line*. Shown in (c) is the fluence spectra after 7 days from the AP9 median (dark blue), AP8 MAX (light blue), and the CRRESPRO Active (green) models. The full set of 7 day MC fluence spectra is shown in (d) with the same color convention as (a)

when a larger quantity of data is used in future versions. Including an MLT dependence should also improve accuracy.

## 6.2 Comparison to Data

Validating AE9/AP9/SPM with independent measurements is a challenge because good data in the radiation belts are scarce and the temptation to include it all in the model is strong. Nevertheless, the temptation was resisted and several data sets were excluded to serve as a check on the final V1.0 product. Data cleaning and cross-calibration of the type discussed in Sect. 4 were not performed on the validation data and the nominal energy channels and geometric factors available publicly or from the instrument Principal Investigators were used without modification. Consequently, comparison of the model predictions to the observations presented in this section should be taken with a grain of salt—the model is certainly not perfect but the data are imperfect as well. Similar to the test suite and model-to-model comparisons, the validation served its purpose by uncovering a number of issues in preliminary versions of AE9/AP9/SPM.

The primary comparisons for AP9 were made with data from the POES/SEM sensor (Evans and Greer 2004). The POES satellites fly in an  $\sim 815$  km, circular,  $98^\circ$  inclination

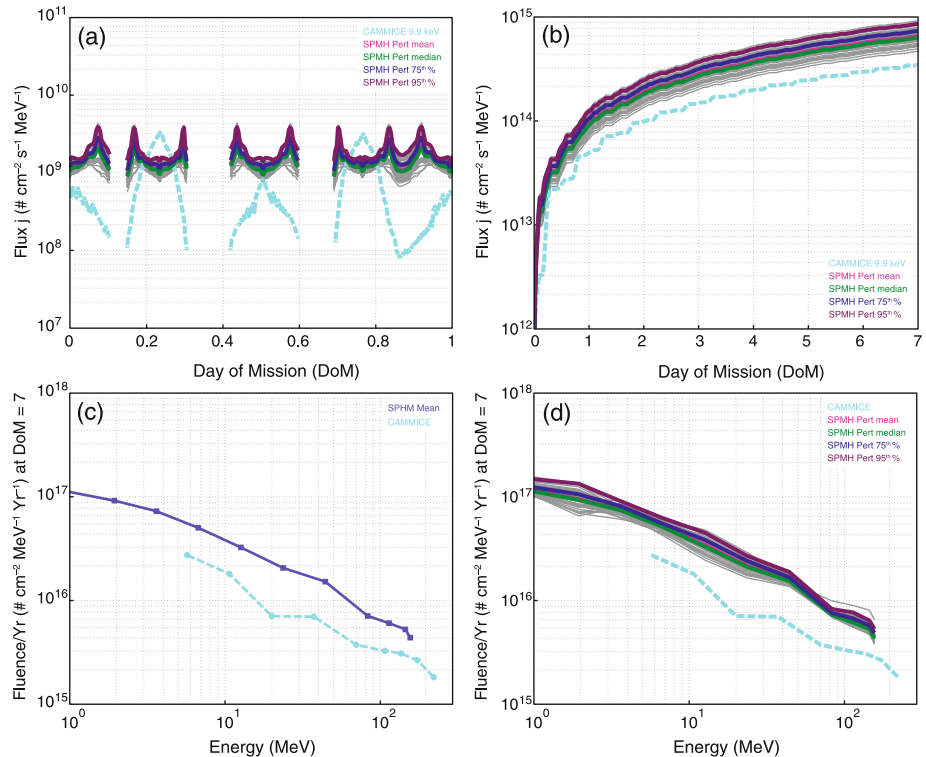


**Fig. 10** Flux (a) and fluence (b) histories of 11.55 keV hydrogen in a GPS orbit from SPMH. See Fig. 8 caption for the color convention. CAMMICE/MICS predictions are shown as the light blue dotted line. Shown in (c) is the fluence spectra after 7 days from the SPMH median (dark blue) and CAMMICE/MICS model (light blue). The full set of 7 day MC fluence spectra is shown in (d) with the same color convention as (a)

orbit and the constellation has been operational since 1978. Data from POES N15 in the 13 year interval from Jul 1998–Dec 2011 were used as illustrated in Fig. 11 showing the  $>36$  MeV channel data in the form of latitude-longitude maps for the median (Fig. 11a) and 95th percentile (Fig. 11c) flux values. Figures 11b and 11d show the corresponding AP9 median and 95th percentile maps, respectively, computed for a 3.5 year interval with 40 MC runs. Computer runtime restrictions precluded a direct 13 year AP9 simulation with 40 MC runs. Agreement is reasonable both in location and intensity with the POES data tending to be somewhat more intense. This can be seen in Fig. 12 where the  $>36$  MeV fluence for each year of the POES data is plotted against one year of AP9 output. Most of the POES curves are between the median and 95th percentile of AP9, and the AP9 median is above the AP8 MIN curve as discussed previously.

AE9 electron flux predictions in LEO were compared to the data from the IDP sensor on the DEMETER satellite which flew in a 660 km, circular,  $98^\circ$  orbit during the period Jan 2005–Dec 2010 (Sauvaud et al. 2006). Figure 13 contains maps of the median and 95th percentile  $>0.322$  MeV electron flux as measured by the DEMETER/IDP over 6 years (Figs. 13a and 13c) and computed from 40 MC AE9 runs for 1 year (Figs. 13b and 13d). The similarity of the general morphology of the SAA and the outer belt horns is comforting but there are some substantial differences. For example, AE9 underpredicts the median in and around the SAA, it overpredicts the 95th percentile in the same areas and it does not

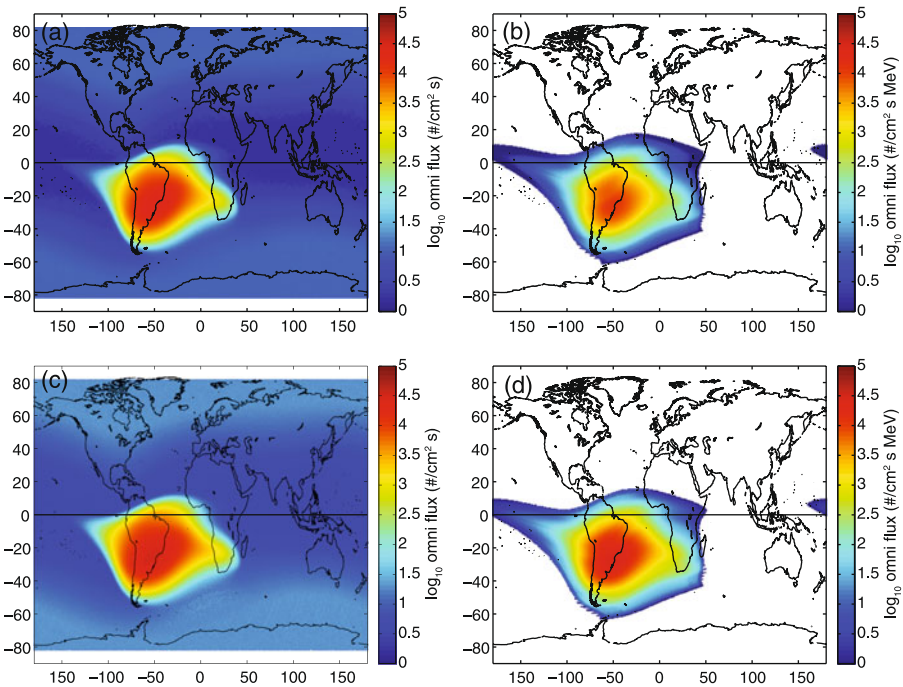
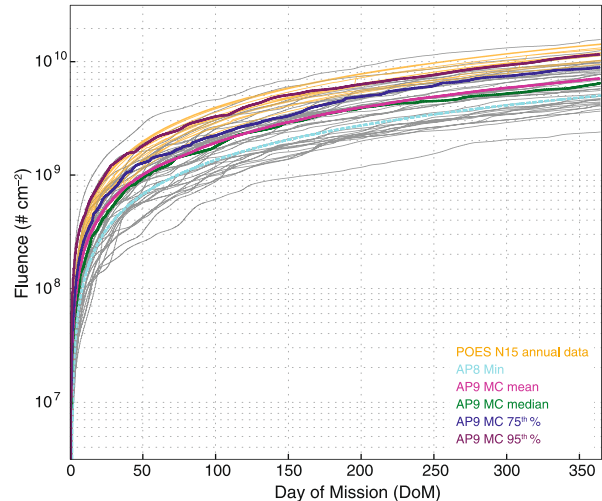


**Fig. 11** Median (a) and 95th percentile (c)  $>36$  MeV flux maps constructed from 13 years of POES N15/SEM data. Similar median (b) and 95th percentile maps (d) determined from 40 MC AP9 scenarios of 3.5 years duration each

**Fig. 12** One year  $>36$  MeV fluence profiles from each of the 13 years of POES/SEM data (*tan lines*) compared to AP9 aggregate predictions and 40 MC scenarios (see Fig. 8 for color code). AP8 MIN is the *light blue line*



capture some of the 95th percentile activity in the slot regions. Indeed, AE9 suffers from a lack of electron data near the SAA manifesting itself through interpolation with templates inspired by CRRES/HEEF/MEA data with TSX5/CEASE and HEO/DOS data at higher ( $K, \Phi$ ) and lower  $h_{min}$  values. Comparing DEMETER/IDP higher energy channels to AE9

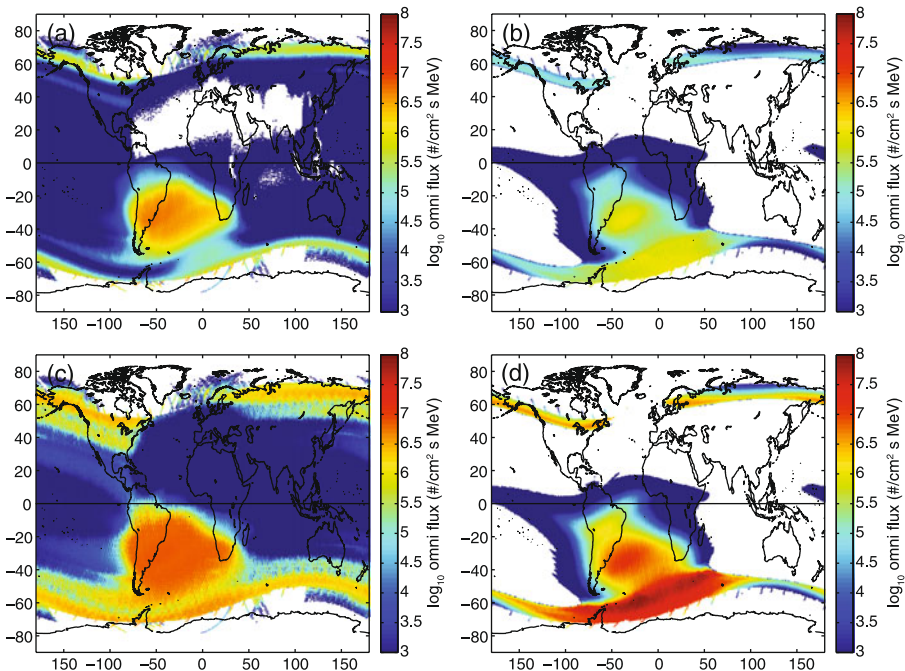


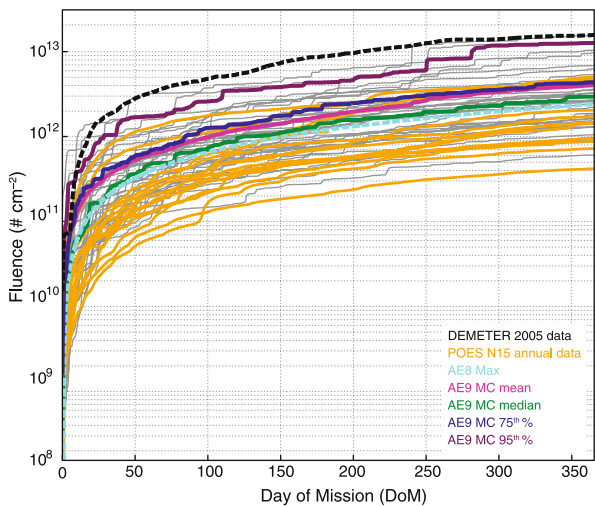
**Fig. 13** Median (a) and 95th percentile (c)  $>0.322$  MeV flux maps determined from 6 years of DEMETER/IDP data. Similar median (b) and 95th percentile maps (d) determined from 40 MC AE9 scenarios each run for 3.5 years

the differences are most apparent in the energy range  $<700$  keV and decrease in magnitude with increasing energy.

The differences are also apparent in the one-year (2005) fluence plot of Fig. 14 where DEMETER/IDP data is compared to AE9 aggregates and AE8 MAX for a  $>300$  MeV equivalent channel estimated by interpolating the IDP  $>0.322$  MeV and  $>0.108$  MeV native channels. Channel interpolation was done to match the  $>0.300$  keV electron channel on the POESN15/SEM which is also shown in Fig. 14. DEMETER/IDP is above the 95th AE9 percentile level while the POES/SEM is near the mean. However, though at a higher altitude of 800 km the POES/SEM fluences are *less* than DEMETER, indicating a large uncertainty in one or both data sets. With contamination always an issue in the proton-rich SAA and detector fields-of-view an issue for pitch-angle distributions peaked near  $90^\circ$  local (Rodger et al. 2010) it is not surprising that in the absence of detailed response function level analysis the data sets do not agree.

At geosynchronous orbit the time step restrictions on AE9/AP9/SPM are relaxed and it is possible to quickly run extended missions. Figure 15 compares AE9 electron fluence over a period of 8.5 years starting in Aug 2001 to measurements from the CEASE sensor on the DSP21 satellite for the  $>0.37$  MeV (Fig. 15a),  $>1.51$  MeV (Fig. 15b) and  $>2.02$  MeV (Fig. 15c). The CEASE sensor is nearly identical to the one flown on TSX5 used in AE9 and has been well studied (Brautigam et al. 2006). Periods of intense solar proton events, a source of contamination, were removed when integrating both the model and data fluxes. Shown in Fig. 15d is the output from the GOES/SEM  $>2$  MeV channel for a period of 10 years starting in Jul 1998 compared to AE9 fluence predictions. Over the nearly solar-cycle length time period, the flux integral over time (= fluence) averages out the dynam-

**Fig. 14** One year  $>0.3$  MeV fluence profiles from the POESN15/SEM data (tan lines) compared to AE9 aggregate predictions and 40 MC scenarios (see Fig. 8 for color code). AE8 MAX is the light blue curve. DEMETER/IDP data is also shown (dotted brown line), albeit measured at a lower altitude



ical variations and the data converges to close to the AE9 median for all channels but the CEASE/DSP21  $>1.51$  MeV channel, where it is close to the 95th level. Not surprisingly the dip in both the CEASE/DSP21 data observed prior to year 2 and the dip in the GOES/SEM data prior to year 7 represent the relatively weak electron environment at GEO during the maximum of Solar Cycle 23 prior to the large buildup on the downside of the solar cycle.

## 7 Summary

The AE9/AP9/SPM V1.0 suite of models represents a transformational approach to specifying the radiation environment for modern satellite design applications. Uncertainties in the model predictions are explicitly included yielding a capability to generate arbitrary percentile flux levels (e.g. mean, median, 95th percentile) from either perturbed mean maps capturing mostly the sensor and data reduction uncertainties, or the full Monte-Carlo autoregressive scheme capturing the statistical space weather variations as well. Included in V1.0 are novel statistical algorithms, spectral inversion techniques, multiple coordinates systems and a diverse set of satellite data cleaned and cross-calibrated to the extent realistically achievable given the development program's finite resources and schedule. Hopefully, the architectural and operational details outlined in this paper are all "under the hood" as far as the design engineer is concerned. Running V1.0 as part of a radiation effects analysis produces a probabilistic assessment that can be traded off at the system level with other bus, payload and mission risks. To a design engineer uncertainty in the environment specification is just uncertainty whether it is rooted in imperfect sensors, interpolation algorithms or the dynamic environment.

There are a number of known issues in the model and, most certainly, issues that have yet to be uncovered. Below is a summary of the major issues, some of which have been previously mentioned:

- There are no reliable data for inner zone electrons at lower energy ( $<\sim 600$  keV). Spectral and spatial extrapolation of the existing data set can lead to large deviations (e.g., comparison to POES and DEMETER data). However, the problem appears to be no worse than in AE8.

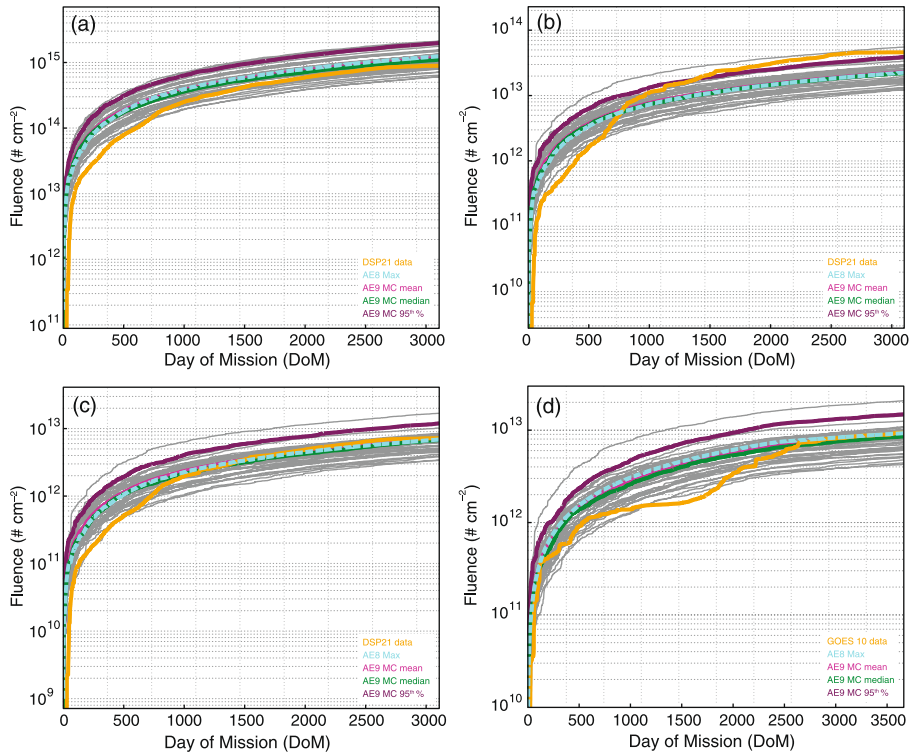


**Fig. 15** Fluence vs time profiles as measured by DSP21/CEASE in GEO over 8.5 years in the (a)  $>0.37$  MeV, (b)  $>1.51$  MeV and (c)  $>2.02$  MeV channels (tan lines) compared to AE9 aggregate predictions and 40 MC scenarios (see Fig. 8 for color code). Panel (d) shows a similar comparison using the  $>2$  MeV measurements from GOES10/SEM over 10 years

- There are no data for high energy protons ( $>\sim 200$  MeV). AP9 goes out to 400 MeV using a physics-based model extrapolation. Lack of high-energy proton data, a regime especially affecting on-board electronics, is the primary reason for flying the Relativistic Proton Spectrometer (RPS) on the Van Allen Probes (Mazur et al. 2012).
- SPMH (plasma hydrogen), SPMHE (plasma helium), SPMO (plasma oxygen) and SPME (plasma electron) models have small error bars which do not adequately reflect the uncertainty in the measurements. There were limited data and spectral smoothness was imposed at the expense of reducing the error bar.
- Errors in the primary flux map variables  $m50$  (log 50th percentile) and  $m95'$  (log 95th–50th percentile) were capped at factors of 100 (electrons) and 10 (protons). Large variations in these quantities can quickly lead to obviously unrealistic variations in fluxes derived from our assumed non-Gaussian Weibull and lognormal distributions. This capping does not limit the representation of space weather variation which is captured in  $m95'$  and the spatiotemporal covariance matrices.
- Run times are slow for large numbers of MC runs, especially for LEO.

To resolve many of these issues and to improve the overall accuracy of the model more data are crucial. The architecture of AE9/AP9/SPM allows for easy incorporation of new data. All that is required is a cleaned, unidirectional differential flux ( $j$ ) data set mapped to the model coordinates along the satellite ephemeris, with an estimate of measurement error ( $d \ln j$ ).

The error can be determined by direct observation and modeling of detector performance or by cross-calibration. This new data set becomes just another element of the collection of all data sets on which the automated process building the flux maps and covariance matrices (denoted together as the “runtime tables”) operates. Much hope is riding on the NASA Van Allen Probe mission to provide a rich set of energetic particle and plasma data from the many well-calibrated instruments of good pitch angle and energy resolution. With two satellites in a GTO orbit slated for 2–4 years of operation the coordinate coverage should be excellent. Van Allen Probe data will be used first to validate the performance of V1.0 before being incorporated into a new version of the model.

Even with the planned future data sets there will always be a need for templates (Sect. 5) to extrapolate and interpolate the data across spectral and spatial coverage gaps. Significant effort went into building the templates (Table 4) used in AE9/AP9/SPM but they are by no means unique. Additional templates based on both empirical and physics-based analysis are needed and can be easily integrated into the flux map bootstrap construction process.

The model is also fundamentally limited in that it does not capture the MLT dependence of the plasma nor the space weather variations on time scales of less than a day. Future versions can remedy the former problem in a straightforward manner by incorporating an MLT coordinate. However, the latter problem is likely beyond the capabilities of the current empirically based statistical algorithms given the required spatial and temporal data coverage. A more promising approach is to build a “sample solar cycle (or cycles)” that attempts to reconstruct past particle flux distributions using data, physics-based models, data-assimilation and other statistical techniques (O’Brien and Guild 2010; Bourdarie et al. 2009). Such a reanalysis could provide an environment with variations on time scales limited only by the fidelity of the physics-based models. A user might then fly a mission through the reference cycle and accumulate model data in order to build the required statistical distribution on any time scale greater than the model resolution. Reanalysis introduces uncertainty through the statistical and physics-based modeling processes in addition to what is already in the data, but such a description might be far better than none when knowledge of the flux statistics for small time-averaged intervals is essential.

Solar proton events were not included in AP9, though they can be the dominant particles providing dose over time periods of hours to days at high altitudes. Merging AP9 with existing statistical models of solar proton events (e.g. Xapsos et al. 1998, 1999) is a worthwhile endeavor which would provide an integrated application of clear value to the satellite design engineers.

Perhaps the most important consideration concerning the future of AE9/AP9/SPM is the necessity of enlisting the effort of other agencies and countries in the development processes. To build a model of the scope of AE9/AP9/SPM V1.0 required a focused effort with a relatively small team and a level of resources that the NRO and AFRL were able to provide. With V1.0 built and released to the public it is the sincere hope of the V1.0 developers that the radiation belt community will eventually take ownership, incorporating new data sets, algorithms (and maybe a new name) to make the model a true global standard.

**Acknowledgements** Many people have been involved in building AE9/AP9/SPM. Much credit is due Clark Groves for getting the project started. The authors especially wish to thank Joe Mazur, Bern Blake, Jim Roeder and Joe Fennell for technical advice on the HEO, ICO and POLAR/CAMMICE data; Richard Selesnick for cleaning and analysis of the SAMPEX/PET and POLAR/HISTp data and for his physics-based proton belt climatology model; Jon Niehof and Jack Scudder for access to their versions of the POLAR/MICS and POLAR/HYDRA data; Jean-Andre Sauvaud for use of the DEMETER data; Don Brautigam, Sébastien Bourdarie, Daniel Boscher, Jay Albert, Kara Perry, Brian Wie and Seth Claudepiere for technical assistance; Bill Olson, Dave Byers, James Metcalf, Michael Starks, Tim Alsruehe and Geoff Reeves for project management; Bob Weigel and Mike Xapsos for ViRBO and LWS-SET website support; Sharon Benedict for graphics

support; Dave Chenette and Michael Bodeau for helping define the requirements; and the “short list” of engineers and scientists who tested the beta versions and provided valuable feedback all along the way. This work was supported through Air Force contracts FA8718-05-C-0036, FA8718-10-C-001, FA8721-05-C-0002 and FA8802-09-C-0001 and NASA grant NNG05GM22G.

## Appendix A: Acronyms

ACE	Advanced Composition Explorer (satellite)
BDDII	Burst Detector Dosimeter II
CAMMICE	Charge and Mass Magnetospheric Ion Composition Experiment
CEASE	Compact Environment Anomaly Sensor
CPME	Charged Particle Measurement Experiment
CRRES	Combined Radiation and Release Experiment (satellite)
DD	Displacement Damage
DEMETER	Detection of Electro-Magnetic Emissions Transmitted from Earthquake Regions (satellite)
Dos	Dosimeter
EPAM	Electron, Proton, and Alpha Monitor
GEO	Geosynchronous Orbit
GPS	Global Positioning System (satellite)
HEEF	High Energy Electron Fluxmeter
HEO-F1	Highly Elliptical Orbit—Flight 1 (satellite)
HEO-F3	Highly Elliptical Orbit—Flight 3 (satellite)
HISTe	High Sensitivity Telescope—electrons
HISTp	High Sensitivity Telescope—protons
HYDRA	Hot Plasma Analyzer
ICO	Intermediate Circular Orbit (satellite)
IGE	International Geostationary Electron (model)
IDP	Instrument for Particle Detection
IPS	Imaging Proton Spectrometer
LANL-GEO	Los Alamos National Laboratory-Geosynchronous Orbit satellite
LEO	Low-Earth Orbit
MEA	Medium Energy Analyzer
MEO	Medium-Earth Orbit
MICS	Magnetospheric Ion Composition Sensor
MPA	Magnetospheric Plasma Analyzer
PET	Proton/Electron Telescope
PROTEL	Proton Telescope
SAMPEX	Solar Anomalous and Magnetospheric Particle Explorer (satellite)
SCATHA	Spacecraft Charging at High Altitudes (satellite)
SC3	High Energy Particle Spectrometer
SEE	Single event effects
SEM	Space Environment Monitor
SOPA	Synchronous Orbit Particle Analyzer
Tel	Telescope
TIROS	Television Infrared Observation Satellite (satellite)
TSX5	Tri-Services Experiment-5 (satellite)

## Appendix B: Construction of the Flux Maps, Principal Components and Time Evolution Matrices

Described in this appendix are the methods used to build the flux maps and components of the auto-regression scheme (Eq. (7)) introduced in Sect. 5 and illustrated in Fig. 5. Much of the theory underlying the V1.0 architecture can be found in O'Brien (2005), O'Brien and Guild (2010) and Johnston et al. (2013). A good deal of statistical analysis is needed to build the autoregressive model and only a cursory overview is given here. Interested readers are referred to Wilks (2006) for information on the basic techniques and O'Brien (2012a) for the application to radiation belt models.

As mentioned in Sect. 5 the statistical quantities tracked in the flux maps are the 50th and the 95th percentile unidirectional flux values  $m_{50}$  and  $m_{95}$ , respectively. Actually, the variable  $m_{95'} = m_{95} - m_{50}$  is used instead of  $m_{95}$  so the restriction that  $m_{95} > m_{50}$  imposed on the analysis takes the simple form  $m_{95'} > 0$ . Hereinafter the ' will be dropped. From these two quantities the entire particle distribution can be determined by assuming a two-parameter functional form for the distribution function.

For each satellite data set the unidirectional flux measurements are sorted into a set of time sequential maps where the spatial bins are defined by the coordinate grid and the time bin for each map is one day for electrons and 7 days for protons. Note that the term “spatial” is used in a general sense to denote all the non-temporal coordinates including energy. For each satellite pass through a spatial bin during the time bin a value for the flux and variance is computed as a weighted average of the  $j$  and  $d \ln j$  measurements during the pass. Weights are determined by the relative values of  $d \ln j$  which themselves are computed from a cross-calibration procedure discussed in Sect. 4.3. Bin pass average values are then averaged for each time bin. These preliminary maps can be spatially sparse as only coordinate bins through which the satellite passes will contain values. With the tracked percentile values defined as the vector  $\underline{\theta} = (m_{50}, m_{95})$  and their deviations about the average  $\bar{\underline{\theta}}$  as  $\delta\underline{\theta} = \underline{\theta} - \bar{\underline{\theta}}$ , the average value and the covariance matrix  $\text{cov}(\delta\underline{\theta})$  are computed for each bin by using a bootstrap technique over the set of time averaged values. With the bootstrap a random selection of time binned values is chosen, with replacement, to equal the original set size. Each selected value is perturbed randomly in a manner constrained by its standard deviation (in a lognormal sense) and the resultant set sorted to obtain a value for  $\bar{\underline{\theta}}_i$  in each spatial bin  $i$  (hereafter the subscript  $i$  will be dropped to avoid notational overload). Repeating this process 200 times yields a distribution of  $\bar{\underline{\theta}}$  estimates that are used to compute an average  $\bar{\underline{\theta}}$  and a  $2 \times 2$  local  $\text{cov}(\delta\underline{\theta})$ . This process is performed for each spatial bin for each sensor data set.

The filling-in procedure using the templates is as follows. A realization of  $\bar{\underline{\theta}}$  on the sparse grid described above is constructed by randomly perturbing the original  $\bar{\underline{\theta}}$  values consistent with a normal distribution characterized by  $\text{cov}(\delta\underline{\theta})$  in each bin. From this realization the quantity  $\Delta\underline{\theta} = \bar{\underline{\theta}} - \underline{\theta}^{(0)}$ , where  $\underline{\theta}^{(0)}$  is the template estimate, is computed. The  $\Delta\underline{\theta}$  grid is filled in first by using energy interpolation and extrapolation, and then applying nearest-neighbor averaged and smoothed before being added to the original sparse  $\bar{\underline{\theta}}$  grid to produce an estimate for the full  $\bar{\underline{\theta}}$  grid. This process is repeated 10 times for each template and the distribution of  $\bar{\underline{\theta}}$  obtained is used to compute a new best estimate of the  $\bar{\underline{\theta}}$  and  $\text{cov}(\delta\underline{\theta})$  over the entire grid for each satellite.

To compute the final  $\bar{\underline{\theta}}$  map, denoted as the generalized vector  $\bar{\underline{\theta}}$  with a single index covering all the ( $E, K, \Phi$  or  $h_{min}$ ) grid, the individual satellite  $\bar{\underline{\theta}}$  maps are averaged with weighting by the standard deviations computed from  $\text{cov}(\delta\underline{\theta})$  in each bin. The maps are then smoothed. The final covariance  $\text{cov}(\delta\underline{\theta})$  is then captured by computing the “anomaly

matrix”  $\mathbf{S}$  where the number of rows in  $\mathbf{S}$  are the number of grid points (i.e. equal to the number of values in  $\underline{\theta}$ ) and each column of  $\mathbf{S}$  is a normalized bootstrap realization of  $\underline{\theta}$  on the grid obtained by selecting a set of random sensor groups, randomly perturbing  $\underline{\theta}$  in each bin assuming a normal distribution of  $\underline{\theta}$  characterized by  $\text{cov}(\delta\underline{\theta})$  and averaging the result. This layer of bootstrapping captures the uncertainties of measurement errors, spatial interpolation and extrapolation and the temporal coverage limitations of a finite set of sensors. By construction,  $\text{cov}(\delta\underline{\theta}) = \mathbf{SS}^T$  where  $T$  represents the transpose operation. Nominally,  $\text{cov}(\delta\underline{\theta})$  would be a very large matrix of size  $N \times N$ , where  $N$  is twice the number of grid points ( $\sim 50,000$  for AE9/AP9). By constructing  $\mathbf{S}$  of 50 bootstrap realizations, a number found to be sufficient, only an  $N \times 50$  matrix need be computed and stored. Singular value decomposition of  $\mathbf{S}$  keeping only the number of dimensions needed to re-compute 90 % of the total variance further reduces the stored matrix size to  $N \times 10$ .

The end result of the process is a flux map  $\underline{\theta}$  of the 50th and 95th percentile unidirectional flux values with the anomaly matrix  $\mathbf{S}$  allowing for computation of the spatial error covariance across the entire grid. With the assumed Weibull or lognormal distribution functions the mean or any percentile level flux can be computed from  $\underline{\theta}$ . Uncertainties in these values can be calculated from  $\text{cov}(\delta\underline{\theta}) = \mathbf{SS}^T$  and represent estimates of the combined uncertainty imposed by imprecise measurements, lack of spatial and temporal coverage, and the templates used for interpolation and extrapolation.

To determine the quantities involved in auto-regression equation (Eq. (7)) it is first necessary to estimate the spatial ( $\Sigma$ ) and spatiotemporal ( $\hat{\mathbf{R}}$ ) covariance matrices for the flux. Although there is certainly considerable error in computing the spatial and spatiotemporal covariance matrices it will be neglected hereinafter because only a low-order model of the dynamics is sought and the uncertainty in the flux values due to measurement and space weather is tracked through flux maps and associated covariance.

The starting point is the set of time-average fluxes in each spatial bin for each satellite. Randomly selecting two bins (possibly from different sensors), we compute a “Gaussian” correlation coefficient at several different time lags. The time-averaged flux values in each bin are transformed to Gaussian-equivalent variables  $z_i$  according to the relation,

$$\Psi(z_{i,k}) = F_i(j_{i,k}) \approx \frac{k}{1 + N_i} \quad (8)$$

where  $\Psi$  (often denoted  $\Phi$  in the statistical literature) is the cumulative distribution of a standard Gaussian with unit variance and a zero average,  $F_i$  is the empirical cumulative distribution within the  $i$ th bin, and  $k$  is the index of the sort list of  $k = 1$  to  $N_i$  fluxes  $j_{i,k}$  within the bin. This transformation is independent of the choice of Weibull or lognormal distributions. By transforming to the Gaussian-equivalent variables the formalism of multivariate normal distributions can be used to develop the autoregressive prediction model. In particular, the spatial and temporal covariance matrices are defined as,

$$\Sigma = \langle \mathbf{z}(t)\mathbf{z}^T(t) \rangle, \quad (9)$$

$$\hat{\mathbf{R}}(\tau) = \langle \mathbf{z}(t)\mathbf{z}^T(t + \tau_k) \rangle, \quad (10)$$

where  $\mathbf{z}$  is the vector of  $z_i$  values spanning the entire grid,  $\tau_k$  is the  $k$ th time lag and the  $\langle \dots \rangle$  notation represents the average. Because of limited spatial and temporal coverage, the initial estimates of the covariance matrices is incomplete. They are filled in using a 100-point nearest neighbors average.

To reduce the substantial storage requirements of what is nominally a  $N \times N$  dimensional matrix a principal component decomposition of  $\Sigma$  is employed, i.e.,

$$\mathbf{z} = \mathbf{Q}\mathbf{q}, \quad (11)$$

$$\Sigma = \mathbf{Q}\mathbf{Q}^T, \quad (12)$$

where  $\mathbf{Q} = [\hat{\mathbf{q}}_1, \hat{\mathbf{q}}_2, \dots, \hat{\mathbf{q}}_{N_q}]$  is a matrix of the  $i = 1, 2, \dots, N_q$  principal component eigenvectors  $\hat{\mathbf{q}}_i$  and  $\mathbf{q}$  is the state vector of principal component amplitudes representing a particular realization of  $\mathbf{z}$ .  $\Sigma$  contains many noise factors, which we remove by excluding any principal component that explains less than 1 % of the variance. Using the remaining  $N_q \sim 10$  principal components the spatiotemporal covariance can be expressed as,

$$\hat{\mathbf{R}}_k = \mathbf{Q}\langle\mathbf{q}(t)\mathbf{q}^T(t - \tau_k)\rangle\mathbf{Q}^T = \mathbf{Q}\mathbf{R}_k\mathbf{Q}^T, \quad (13)$$

where  $\mathbf{R}_k = \langle\mathbf{q}(t)\mathbf{q}^T(t - \tau_k)\rangle$ . When  $k = 0$  then  $\tau_k = 0$  by definition and  $\mathbf{R} = \mathbf{I}$ , the identity matrix, so that  $\mathbf{R}_0 = \Sigma$ . In summary, the procedure to obtain the spatiotemporal covariance matrices from the data is to (a) compute elements of  $\Sigma$  and each  $\hat{\mathbf{R}}$  from time averages in spatial bins (Eqs. (9) and (10)), (b) fill in the missing elements of  $\Sigma$  and  $\hat{\mathbf{R}}$  via nearest neighbors averaging, (c) determine the principal components  $\mathbf{Q}$  of  $\Sigma$  (Eq. (12)), and (d) determine each  $\mathbf{R}_k$  using Eq. (13).

The autoregressive time-evolution equation (Eq. (7)) of order  $N_G$  is used to advance the  $N_q$  principal component amplitudes in time. An expression for the expectation value  $\langle\mathbf{q}(t)\mathbf{q}^T(t - \tau)\rangle$  can be derived from the time-evolution equation,

$$\langle\mathbf{q}(t)\mathbf{q}^T(t - \tau_m)\rangle = \mathbf{R}_m = \sum_{k=1}^{N_G} \mathbf{G}_k \mathbf{R}_{m-k} + \begin{cases} \mathbf{C}\mathbf{C}^T, & m = 0 \\ 0, & \text{otherwise} \end{cases} \quad (14)$$

where  $\mathbf{R}_{m-k} = \langle\mathbf{q}(t - \tau_m)\mathbf{q}^T(t - \tau_k)\rangle$  and the  $\mathbf{CC}^T$  term arises from  $\langle\eta(t)\mathbf{q}^T(t)\rangle$  because  $\eta(t)$  is uncorrelated with all prior  $\mathbf{q}(t)$ . With the  $\mathbf{R}$  matrices determined from the data, Eq. (14) can be inverted to obtain  $\mathbf{G}$  and  $\mathbf{C}$  (O'Brien 2012a).

Statistically realistic flux profiles are generated by choosing at  $t = 0$  a scenario-specific random seed which determines the initial principal component amplitudes  $\mathbf{q}(0)$  and a set of flux conversion parameters, i.e. the  $\underline{\theta}$  percentiles characterizing the distribution computed from the flux map  $\bar{\theta}$  with a random perturbation added consistent with the global spatial error covariance  $\text{cov}(\delta\theta)$  encoded in the anomaly matrix  $\mathbf{S}$ . A time history of the  $\mathbf{q}(t)$  is generated with Eq. (7), the Gaussian equivalent fluxes  $\mathbf{z}(t)$  determined from Eq. (11) and the physical flux values  $\mathbf{j}(t)$  from the left-side of Eq. (8) using the conversion parameters given by  $\underline{\theta}$ .

## References

- T.W. Armstrong, B.L. Colborn, Evaluation of trapped radiation model uncertainties for spacecraft design, NASA/CR-2000-210072, 2000
- D.M. Boscher, S.A. Bourdarie, R.H.W. Friedel, R.D. Belian, Model for the geostationary electron environment: POLE. IEEE Trans. Nucl. Sci. **50**, 2278–2283 (2003)
- S.A. Bourdarie et al., PRBEM data analysis procedure V1.2, COSPAR Panel on Radiation Belt Environment Modeling (PRBEM), 2008, available at [http://craterre.oncerf.fr/prbem/Data\\_analysis.pdf](http://craterre.oncerf.fr/prbem/Data_analysis.pdf)
- S.A. Bourdarie, A. Sicard-Piet, R. Friedel, T.P. O'Brien, T. Cayton, B. Blake, D. Boscher, D. Lazaro, Outer electron belt specification model. IEEE Trans. Nucl. Sci. **56**, 2251–2257 (2009)
- D.H. Brautigam, CRRES in review: space weather and its effects on technology. J. Atmos. Sol.-Terr. Phys. **64**, 1709–1721 (2002)
- D.H. Brautigam, J. Bell, CRRESELE documentation, PL-TR-95-2128, ADA 301770, Air Force Research Laboratory, Hanscom AFB, MA, 1995
- D.H. Brautigam, M.S. Gussenhoven, E.G. Mullen, Quasi-static model of outer zone electrons. IEEE Trans. Nucl. Sci. **39**, 1797–1803 (1992)

- D.H. Brautigam, K.P. Ray, G.P. Ginnet, D. Madden, Specification of the radiation belt slot region: comparison of the NASA AE8 model with TSX5/CEASE data. *IEEE Trans. Nucl. Sci.* **51**, 3375–3380 (2004)
- D.H. Brautigam, B. Dichter, S. Woolf, E. Holeman, A. Ling, D. Wrazen, Compact environmental anomaly sensor (CEASE): response functions, AFRL-VS-HATR-2006-1030, Air Force Research Laboratory, 2006
- J. Cabrera, J. Lemaire, Using invariant altitude (hinv) for mapping of the radiation belt fluxes in the low-altitude environment. *Space Weather* **5**, S04007 (2007). doi:[10.1029/2006SW000263](https://doi.org/10.1029/2006SW000263)
- T.C. Cayton, Objective comparison of CRRES MEA electron spectra using response functions for the SOPA aboard S/C 1989-046, LA-UR-07-8023, Los Alamos National Laboratory, Los Alamos, NM, 2007
- T.E. Cayton, R.D. Belian, Numerical modeling of the synchronous orbit particle analyzer (SOPA, Version 2) the Flew on S/C 1990-095, Los Alamos Technical Report, LA-14335, Los Alamos National Laboratory, Los Alamos, NM, 2007
- Y. Chen, R.H.W. Friedel, G.D. Reeves, T. Onsager, M.F. Thomsen, Multisatellite determination of the relativistic electron phase space density at geosynchronous orbit: methodology and results during geomagnetically quiet times. *J. Geophys. Res.* **110**, A10210 (2005). doi:[10.1029/2004JA010895](https://doi.org/10.1029/2004JA010895)
- E.J. Daly, J. Lemaire, D. Heynderickx, D.J. Rodgers, Problems with models of the radiation belts. *IEEE Trans. Nucl. Sci.* **43**, 403–415 (1996)
- B.K. Dichter, F.A. Hanser, B. Sellers, J.L. Hunerwadel, High energy electron fluxmeter. *IEEE Trans. Nucl. Sci.* **40**, 242–245 (1993)
- B. Efron, R. Tibshirani, *An Introduction to the Bootstrap* (Chapman & Hall/CRC, Boca Raton, 1993)
- D. Evans, M.S. Greer, Polar orbiting environmental satellite space environment monitor—2. Instrument descriptions and archive data documentation, NOAA Tech. Mem. 1.4, Space Environ. Lab., Boulder, CO, 2004
- M. Evans, N. Hastings, B. Peacock, *Statistical Distributions*, 3rd edn. (Wiley, Hoboken, 2000)
- J.F. Fennell, J.B. Blake, D. Heynderickx, N. Crosby, HEO observations of the radiation belt electron fluxes: comparison with model predictions and a source for model updates. *Eos Trans. AGU* **84**, #SH52A-05 (2003)
- R.H.W. Friedel, S. Bourdarie, T. Cayton, Intercalibration of magnetospheric energetic electron data. *Space Weather* **3**, S09B04 (2005). doi:[10.1029/2005SW000153](https://doi.org/10.1029/2005SW000153)
- S.F. Fung, Recent developments in the NASA trapped radiation models, in *Radiation Belts: Models and Standards*, ed. by J.F. Lemaire, D. Heynderickx, D.N. Baker. *Geophys. Monogr. Ser.*, vol. 97 (AGU, Washington, 1996), pp. 79–91
- G.P. Ginnet, T.P. O'Brien, AE-9/AP-9 trapped radiation and plasma models requirements specification, Aerospace Technical Report, TOR-2010(3905)-3, 2010
- G.P. Ginnet, S.L. Huston, C.J. Roth, T.P. O'Brien, T.B. Guild, The trapped proton environment in Medium Earth Orbit (MEO). *IEEE Trans. Nucl. Sci.* **57**, 3135–3142 (2010)
- G. Ginnet, T. O'Brien, J. Mazur, C. Groves, W. Olson, G. Reeves, AE(P)-9: the next generation radiation specification models, in *Proceedings of the GOMACTech-08 Conference*, 17–20 March, Las Vegas, NV (2008)
- G.P. Ginnet, B.K. Dichter, D.H. Brautigam, D. Madden, Proton flux anisotropy in low Earth orbit. *IEEE Trans. Nucl. Sci.* **54**, 1975–1980 (2007)
- GOES I-M Data Book, DRL 101-0801 ed. Space Systems Loral, Aug. 31, 1996, GOES/SEM information [online]. Available: <http://rsd.gsfc.nasa.gov/goes/text/goes.databook.html>
- T. Guild, T.P. O'Brien, J. Mazur, M. Looper, On-orbit inter-calibration of proton observations during solar particle events, Aerospace Report No. TOR-2007(3905)-22, Aerospace Corporation, 2009
- M.S. Gussenhoven, E.G. Mullen, M.D. Violet, C. Hein, J. Bass, D. Madden, CRRES high energy proton flux maps. *IEEE Trans. Nucl. Sci.* **40**(6), 1450–1457 (1993)
- M.S. Gussenhoven, E.G. Mullen, D.H. Brautigam, Near-Earth radiation model deficiencies as seen on CRRES. *Adv. Space Res.* **14**, 927–941 (1994)
- F.A. Hanser, Analyze data from CRRES payloads AFGL-701/Dosimeter and AFGL-701-4/Fluxmeter, PL-TR-95-2103, Phillips Laboratory, AFMC, Hanscom AFB, MA, 1995
- D. Heynderickx, M. Kruglanski, V. Pierrard, J. Lemaire, M.D. Looper, J.B. Blake, A low altitude trapped proton model for solar minimum conditions based on SAMPEX/PET data. *IEEE Trans. Nucl. Sci.* **46**, 1475–1480 (1999)
- S.L. Huston, Space environment and effects: trapped proton model, NASA/CR-2002-211784, NASA Marshall Spaceflight Center, Huntsville, AL, 2002
- S.L. Huston, G.A. Kuck, K.A. Pfitzer, Low altitude trapped radiation model using TIROS/NOAA data, in *Radiation Belts: Models and Standards*, ed. by J.F. Lemaire, D. Heynderickx, D.N. Baker. *Geophys. Monogr. Ser.*, vol. 97 (AGU, Washington, 1996), pp. 119–124
- S. Huston, G. Ginnet, T.P. O'Brien, T. Guild, D. Madden, R. Friedel, AE/AP-9 radiation specification model: an update, in *Proceedings of the GOMACTech-08 Conference*, 17–18 March, Orlando, FL (2009)

- IGRF, The international geomagnetic reference field, 2012. Available at <http://www.ngdc.noaa.gov/IAGA/vmod/>
- IRBEM, The international radiation belt environmental modeling library, 2012. Available at <http://irbem.svn.sourceforge.net/viewvc/irbem/web/index.html>
- C.E. Jordan, Empirical models of the magnetospheric magnetic field. *Rev. Geophys.* **32**, 139–157 (1994)
- W.R. Johnston, C.D. Lindstrom, G.P. Ginet, Characterization of radiation belt electron energy spectra from CRRES observations, Abstract #SM33C-1925, American Geophysical Union Fall Meeting, San Francisco, CA, 2010
- W.R. Johnston, C.D. Lindstrom, G.P. Ginet, CRRES medium electron sensor A (MEA) and high energy electron fluxmeter (HEEF): cross-calibrated data set, AFRL, 2011, available at <ftp://virbo.org/johnston/crres/MEAHEEFCC.pdf>
- W.R. Johnston et al., AE9/AP9/SPM radiation environment model, Technical Documentation, in preparation to be released as an Air Force Research Laboratory Technical Report, 2013
- J. Koller, S. Zaharia, LANL\* V2.0: global modeling and validation. *Geosci. Model Dev.* **4**, 669–675 (2011). doi:[10.5194/gmd-4-669-2011](https://doi.org/10.5194/gmd-4-669-2011)
- J. Koller, G.D. Reeves, R.H.W. Friedel, LANL\* V1.0: a radiation belt drift shell model suitable for real-time and reanalysis applications. *Geosci. Model Dev.* **2**, 113–122 (2009)
- H.C. Koons, J.E. Mazur, R.S. Selesnick, J.B. Blake, J.F. Fennell, J.L. Roeder, P.C. Anderson, The impact of the space environment on space systems, in *6th Spacecraft Charging Technology Conference*, AFRL Tech. Report No. AFRL-VS-TR-20001578, pp. 7–11, Air Force Research Laboratory, Hanscom AFB, MA, 2000
- J.-M. Lauenstein, J.L. Barth, D.G. Sibeck, Toward the development of new standard radiation belt and space plasma models for spacecraft engineering. *Space Weather* **3**, S08B03 (2005). doi:[10.1029/2005SW000160](https://doi.org/10.1029/2005SW000160). Presentations from the workshop are available online at [http://lwsscience.gsfc.nasa.gov/RB\\_meeting1004.htm](http://lwsscience.gsfc.nasa.gov/RB_meeting1004.htm)
- A.M. Lenchek, S.F. Singer, Effects of the finite gyroradii of geomagnetically trapped protons. *J. Geophys. Res.* **67**, 4073–4075 (1962)
- J. Mazur, L. Friesen, A. Lin, D. Mabry, N. Katz, Y. Dotan, J. George, J.B. Blake, M. Looper, M. Redding, T.P. O'Brien, J. Cha, A. Birkitt, P. Carranza, M. Lalic, F. Fuentes, R. Galvan, M. McNab, The relativistic proton spectrometer (RPS) for the radiation belt storm probes mission. *Space Sci Rev.* (2012, this issue). doi:[10.1007/s11214-012-9926-9](https://doi.org/10.1007/s11214-012-9926-9)
- J.P. McCollough, J.L. Gannon, D.N. Baker, M. Gehmeyr, A statistical comparison of commonly used external magnetic field models. *Space Weather* **6**, S10001 (2008). doi:[10.1029/2008SW000391](https://doi.org/10.1029/2008SW000391)
- C.E. McIlwain, Coordinates for mapping the distribution of magnetically trapped particles. *J. Geophys. Res.* **6**, 3681 (1961)
- J.D. Meffert, M.S. Gussenhoven, CRRESPRO documentation, PL-TR-94-2218, ADA 284578, Phillips Laboratory, Hanscom AFB, MA, 1994
- A. Milillo, S. Orsini, I.A. Daglis, Empirical model of proton flux in the equatorial inner magnetosphere: development. *J. Geophys. Res.* **106**, 25713–25729 (2001)
- J. Niehof, Diamagnetic cavities and energetic particles in the Earth's magnetospheric cusps. PhD Thesis, Boston University, 2011
- T.P. O'Brien, A framework for next-generation radiation belt models. *Space Weather* **3**, S07B02 (2005). doi:[10.1029/2005SW000151](https://doi.org/10.1029/2005SW000151)
- T.P. O'Brien, Documentation of C inversion library, 2010, available as part of IRBEM-LIB at <http://irbem.svn.sourceforge.net/viewvc/irbem/web/index.html>
- T.P. O'Brien, Adding multiple time lags to AE9/AP9 V1.0, Aerospace Report No. TOR-2012(1237)-3, 2012a
- T.P. O'Brien, Data cleaning guidelines for AE-9/AP-9 data sets, Aerospace Report No. TOR-2012(1237)-4, 2012b
- T.P. O'Brien, T.B. Guild, Trapped electron model 2 (TEM-2), Aerospace Report No. TR-2010(3905)-2, Aerospace Corporation, El Segundo, CA, 2010
- W.P. Olson, K.A. Pfitzer, Magnetospheric magnetic field modeling, Annual Scientific Report, Air Force Office of Scientific Research contract F44620-75-C-0033, McDonnell Douglas Astronautics Co., Huntington Beach, CA, 1977
- W.H. Press, S.A. Teukolsky, W.T. Vetterling, B.P. Flannery, *Numerical Recipes in C*, 2nd edn. (Cambridge University Press, Cambridge, 1992)
- Radiation models for engineering and operations, session at the 2007 NOAA Space Weather Workshop. Presentations from the workshop are available at: <http://helios.sec.noaa.gov/sww/index.html>, 2007
- Radiation Specifications Forum, 2007. Website at: <http://lws-set.gsfc.nasa.gov/RadSpecsForum.htm>
- G.D. Reeves, Y. Chen, G.S. Cunningham, R.W.H. Friedel, M.G. Henderson, V.K. Jordanova, J. Koller, S.K. Morley, M.F. Thomsen, S. Zaharia, Dynamic radiation environment assimilation model: DREAM. *Space Weather* **10**, S03006 (2012). doi:[10.1029/2011SW000729](https://doi.org/10.1029/2011SW000729)

- C.J. Rodger et al., Use of POES SEM-2 observations to examine radiation belt dynamics and energetic electron precipitation into the atmosphere. *J. Geophys. Res.* **115**, A04202 (2010). doi:[10.1029/2008JA014023](https://doi.org/10.1029/2008JA014023)
- J.L. Roeder, M.W. Chen, J.F. Fennell, R. Friedel, Empirical models of the low-energy plasma in the inner magnetosphere. *Space Weather* **3**, S12B06 (2005). doi:[10.1029/2005SW000161](https://doi.org/10.1029/2005SW000161)
- J.G. Roederer, *Dynamics of Geomagnetically Trapped Radiation* (Springer, New York, 1970)
- C.J. Roth et al., AE9/AP9/SPM radiation environment model. User's guide, in preparation to be released as an Air Force Research Laboratory Technical Report, 2013
- J.A. Sauvaud, T. Moreau, R. Maggiolo, J.-P. Treilhou, C. Jacquay, A. Cros, J. Coutelier, J. Rouzaud, E. Penou, M. Gangloff, High-energy electron detection onboard DEMETER: the IDP spectrometer, description and first results on the inner belt. *Planet. Space Sci.* **54**, 502–511 (2006)
- D.M. Sawyer, J.I. Vette, AP-8 trapped proton model environment for solar maximum and minimum, NSSDC/WDC-A-R&S 76-06, Natl. Space Sci. Data Cent., Greenbelt, MD, 1976
- M. Schulz, Canonical coordinates for radiation belt modeling, in *Radiation Belts: Models and Standards*, ed. by J.F. Lemaire, D. Heynderickx, D.N. Baker. *Geophys. Monogr. Ser.*, vol. 97 (AGU, Washington, 1996), pp. 153–160
- R.S. Selesnick, M.D. Looper, R.A. Mewaldt, A theoretical model of the inner proton radiation belt. *Space Weather* **5**, S04003 (2007). doi:[10.1029/2006SW00275](https://doi.org/10.1029/2006SW00275)
- S.M. Seltzer, Updated calculations for routine space-shielding radiation dose estimates: SHIELDOSE-2. Gaithersburg, MD, NIST Publication NISTIR 5477, 1994
- V.P. Shabansky, Some processes in the magnetosphere. *Space Sci. Rev.* **12**(3), 299–418 (1971)
- A. Sicard-Piet, S. Bourdarie, D. Boscher, R.H.W. Friedel, M. Thomsen, T. Goka, H. Matsumoto, H. Koshiishi, A new international geostationary electron model: IGE-2006, from 1 keV to 5.2 MeV. *Space Weather* **6**, S07003 (2008). doi:[10.1029/2007SW000368](https://doi.org/10.1029/2007SW000368)
- J.D. Sullivan, Geometrical factor and directional response of single and multi-element particle telescopes. *Nucl. Instrum. Methods* **95**(1), 5–11 (1971)
- M.F. Thomsen, D.J. McComas, G.D. Reeves, L.A. Weiss, An observational test of the Tsyganenko (T89a) model of the magnetic field. *J. Geophys. Res.* **101**, 24827–24836 (1996)
- M.F. Thomsen, M.H. Denton, B. Lavraud, M. Bodeau, Statistics of plasma fluxes at geosynchronous orbit over more than a full solar cycle. *Space Weather* **5**, S03004 (2007). doi:[10.1029/2006SW000257](https://doi.org/10.1029/2006SW000257)
- A.L. Vampola, The ESA outer zone electron model update, in *Environment Modelling for Space-Based Applications, Symposium Proceedings (ESA SP-392)*, ed. by W. Burke, T.-D. Guyenne, 18–20 September 1996 (ESTEC, Noordwijk, 1996), p. 151
- J.I. Vette, The NASA/National Space Science Data Center Trapped Radiation Environment Model Program (TREMP) (1964–1991), NSSDC/WDC-A-R&S 91-29, Natl. Space Sci. Data Cent., Greenbelt, MD, 1991a
- J.I. Vette, The AE-8 trapped electron model environment, NSSDC/WDC-A-R&S 91-24, NASA Goddard Space Flight Center, Greenbelt, MD, 1991b
- D.S. Wilks, *Statistical Methods in the Atmospheric Sciences*, 2nd edn. (Academic Press, Burlington, 2006)
- G.L. Wrenn, A.J. Sims, Internal charging in the outer zone and operational anomalies, in *Radiation Belts: Models and Standards*, ed. by J.F. Lemaire, D. Heynderickx, D.N. Baker. *Geophys. Monogr. Ser.*, vol. 97 (AGU, Washington, 1996), pp. 275–278
- M.A. Xapsos, G.P. Summers, E.A. Burke, Probability model for peak fluxes of solar proton events. *IEEE Trans. Nucl. Sci.* **45**(6), 2948–2953 (1998)
- M.A. Xapsos, G.P. Summers, J.L. Barth, E.G. Stassinopoulos, E.A. Burke, Probability model for worst case solar proton event fluences. *IEEE Trans. Nucl. Sci.* **46**(6), 1481–1485 (1999)